Mapping High-Resolution Global Impervious Surface Area: Status and Trends

Huiqun Ren, Yu Liu, Xiaoyu Chang, Jie Yang, Xiao Xiao, and Xin Huang, *Senior Member, IEEE*

***Abstract*—Impervious surface area (ISA) mapping at the global scale has entered a new era. Currently, the number of high-resolution global ISA products is gradually increasing; however, a literature review that systematically investigates these ISA products is still lacking, which limits the application of these products. Thus, we provide a comprehensive analysis of the existing high-resolution global ISA products, concentrating on the aspects of the data sources, training samples, features, and methods. Moreover, we evaluate these products at multitemporal and multispatial scales, using a series of independent test samples. The results demonstrate that the multitemporal accuracy of the ISA products presents an increasing trend, due to the increase of the available sensors. Among the continuous time-series products [e.g., the updated new global impervious surface area (GISA 2.0), the global impervious surface area (GISA), global annual urban dynamics, global human settlement layer, and global artificial impervious areas], the accuracy of the GISA 2.0 outperforms the others at global, continental, and regional scales. However, the mapping performance of these products in small towns and arid and rural regions needs to be enhanced. In particular, we focus on the spatio-temporal disagreement of the ISA products. We show that the high disagreement regions are predominantly concentrated in eastern Asia, western Europe, and eastern North America. In addition, the high disagreement regions are characterized by low ISA density, high vegetation coverage, and high albedo bare ground coverage. Additionally, this article concludes with some remarks about the future directions of global ISA mapping.**

***Index Terms*—Global, high resolution, impervious surface, Landsat, remote sensing, sentinel, urban.**

Manuscript received 14 June 2022; revised 23 July 2022; accepted 19 August 2022. Date of publication 24 August 2022; date of current version 8 September 2022. This work was supported in part by the National Natural Science Foundation of China under Grant 41971295 and in part by the Foundation for the Innovative Research Groups of the Natural Science Foundation of Hubei Province under Grant 2020CFA003. *(Corresponding authors: Yu Liu; Xin Huang.)*

Huiqun Ren and Jie Yang are with the School of Remote Sensing and Information Engineering, Wuhan University, Wuhan 430079, China (e-mail: hqunren@whu.edu.cn; yang9tn@163.com).

Yu Liu is with the Key Laboratory of Aerospace Information Application, CETC, Shijiazhuang 050000, China, and also with the School of Artificial Intelligence, Xidian University, Xi'an 710071, China (e-mail: liuyu@stu.xidian.edu.cn).

Xiaoyu Chang is with the Key Laboratory of Aerospace Information Application, CETC, Shijiazhuang 050000, China (e-mail: lightraincxy@163.com).

Xiao Xiao is with the Spatial Information Technology Application Department, Changjiang River Scientific Research Institute, Wuhan 430010, China (e-mail: xiaoxiao@126.com).

Xin Huang is with the School of Remote Sensing and Information Engineering, and State Key Laboratory of Information Engineering in Surveying, Mapping and Remote Sensing, Wuhan University, Wuhan 430079, China (e-mail: huang_whu@163.com).

Digital Object Identifier 10.1109/JSTARS.2022.3201380

I. Introduction

IMPERVIOUS surface areas (ISAs) are usually covered by man-made materials that prevent water penetrating into soil. They usually include buildings, roads, roofs, etc. [1], [2]. In the past decades, urbanization has been growing rapidly throughout the world, especially in developing countries such as China and India. Although urbanization has brought convenience to mankind, it has also led to climate, topographic, and ecological problems, e.g., urban heat islands, soil erosion, and air pollution [3], [4], [5]. The emergence of ISA products has provided new indicators for measuring human activity intensity, reflecting the urban development process and monitoring environmental quality [6], [7]. Furthermore, the mapping or estimation of ISA can help with the monitoring of population growth, urban expansion, and environmental change [8], [9], [10]. Global ISA mapping can provide reliable macroscopic information on global social, economic, and ecological factors, and is thus of great importance.

From the 1970s to the 1980s, the main means of extracting ISA information was traditional surveying technology, such as field surveys, and aerial photo interpretation. Although the traditional surveying technology can offer accurate and reliable information on impervious surfaces, ISA mapping using the traditional surveying technology is limited in scope (i.e., limited to regional or local scales), expensive, and cannot easily be used to update datasets in a timely manner [11]. From the economic and technical point of view, traditional surveying technology is not suitable for mapping ISA datasets at a global scale. The remote sensing technology offers a new approach, with a high cost–benefit ratio, to mapping global ISA products. However, in the early years (i.e., the 1990s), the advancement of global ISA mapping was hindered by the poor availability of remote sensing images [12]. Up until the year 2000, there was only one map—The Digital Chart of the World (DCW or VMAP0)—that described the global urban areas [13]. The DCW product, as the earliest available global urban extent map with a scale of 1:1000000, represents the beginning of mapping global ISA.

The period from the 2000s to the 2010s was a stage of development for global ISA mapping. During this time, satellite imagery and remote sensing techniques started to gain popularity for the mapping of global ISA datasets, and some products related to ISA (the so-called first-generation products) were produced by various organizations. Examples of the first-generation ISA products are the History Database of the Global Environment v3 (HYDE3) with a 10-km resolution

TABLE I
HIGH-RESOLUTION GLOBAL IMPERVIOUS SURFACE AREA PRODUCTS CONSIDERED IN THIS RESEARCH

Abbr.	Map (reference)	Data sources	Spatial resolution	Time span(year)	Definition	Mapping method
GISA 2.0	A updated Global impervious surface area [38]	Landsat TM, ETM+, and OLI, DEM	30 m	1985–2018	Impervious surface area	RF
GISA	Global impervious surface area [37]	Landsat TM, ETM+, and OLI, DEM	30 m	1972–2019	Impervious surface area	Local adaptive RF
GAIA	Global artificial impervious areas [35]	Landsat TM, ETM+, and OLI, Sentinel-1, VIIRS NTL, MODIS	30 m	1985–2018	Artificial impervious areas	Exclusion-inclusion method
GAUD	Global annual urban dynamics [36]	Landsat TM, ETM+, and OLI, DMSP-OLS NTL	30 m	1985–2015	Urban areas	RF, temporal segmentation
GHSL	Global Human Settlement Layer [32], [33], [34]	Landsat MSS, TM, ETM+, and OLI	30 m	1975,1990, 2000,2014	Built-up area	SML
		Sentinel-1	20 m	2016		SML
		Sentinel-2	10 m	2018		Convolutional neural network
GlobeLand30	30 m Global Land Cover product [45]	Landsat TM and ETM, OLI, HJ-1	30 m	2000,2010, 2020	Artificial surfaces	POK-based method
FROM-GLC 2010	Finer Resolution Observation and Monitoring of Global Land Cover product [29], [30], [31]	Landsat TM and ETM+	30 m	2010	Impervious	MLC, J4.8 decision tree classifier, RF, SVM
		Landsat OLI	30 m	2015		RF
		Landsat, Sentinel-2, SRTM DEM	10 m/30 m	2017		RF
MSMT_2015 or GLC_FCS30-2015	Multi-source multi-temporal impervious surface map [40]	Landsat OLI, Sentinel-1, VIIRS NTL, SRTM DEM	30 m	2015	Impervious surface area	Local adaptive RF
GLC_FCS30-2020	Global land cover product with fine classification system [39]	Landsat, Sentinel-1, VIIRS NTL, DEM	30 m	2020		Local adaptive RF

Note: Long time-series (i.e., more than 30 year) Global ISA datasets include GISA 2.0, GISA, GAIA, GAUD, and GHSL. Others datasets are refereed to short time-series (i.e., less than 30 year) Global ISA datasets. In this paper, MSMT_2015 is also called GLC_FCS30-2015 because they were derived by the same method. Hence, GLC_FCS30-2015 and GLC_FCS30-2020 is hereafter referred to as the "GLC_FCS30" datasets. Abbreviations: MSS, Multispectral Scanner; TM, Thematic Mapper; ETM+, Enhanced Thematic Mapper Plus; OLI, Operational Land Imager; DEM, digital elevation model; VIIRS, Visible Infrared Imaging Radiometer Suite; NTL, nighttime light; MODIS, Moderate Resolution Imaging Spectroradiometer; DMSP-OLS, Defense Meteorological Satellite Program's Operational Line-scan System; HJ-1, the Chinese Environmental and Disaster satellite; SRTM, Shuttle Radar Topography Mission; RF, random forest; SML, symbolic machine learning model; POK-based method, the pixel-object-knowledge-based method; MLC, conventional maximum likelihood classifier; SVM, support vector machine.

[14], LandScan 2005 (LSCAN) [15], the Global Rural-Urban Mapping Project (GRUMP) [2], [16], Global Land Cover 2000 (GLC 2000) at a 1-km resolution [17], the Moderate Resolution Imaging Spectroradiometer (MODIS) 500-m map of global urban extent (MCD12Q1) [18], [19], GlobeCover [20], and the European Space Agency Climate Change Initiative Land Cover project (ESA-CCI-LC) with a spatial resolution of 300 m [21]. These datasets were generated from coarse spatial resolution ($>$ 30 m) remote sensing data, and built with the aid of the DCW product, vector maps, and population data [22], [23]. Although the first-generation products have significant value for various applications and policy decisions, they also suffer from some issues, i.e., the coarse resolution, limited accuracy, and disagreement between products [24], [11].

During the 2000s to 2010s, the first-generation datasets evolved from simple data processing (e.g., fusion, clustering) and regression analysis to supervised–unsupervised classification and feature extraction. This demonstrates that remote sensing technology was gradually being employed in global ISA mapping. However, the first-generation datasets exhibited serious misclassification and overestimation problems, due to the fact that only spectral features were considered and/or coarse-resolution images were used. Furthermore, the intrinsic characteristics of ISA, including the complexity, diversity, and heterogeneity, increases the difficulty of accurate detection from remote sensing images. Hence, there is an urgent need to develop a global ISA dataset that has a high spatial resolution ($\leq$ 30 m) and precise mapping performance for accurate and efficient monitoring.

The period from 2010 has been a boom period for global ISA mapping. With the advent of freely available high-resolution ($\leq$ 30 m) Earth observation satellite images, such as Landsat and Sentinel, much effort has been made with regard to global ISA mapping. High-resolution images with rich spectral, spatial, and texture information hold great potential for precise and accurate global ISA mapping. Moreover, the emergence of cloud computing platforms [such as Google Earth Engine (GEE), Amazon Web Services (AWS), Microsoft Azure Cloud, and PIE-Engine] has enabled parallel accessing, processing, and computing of huge amounts of remote sensing data [25]. Global ISA datasets with a high resolution ($\leq$ 30 m) (the so-called second-generation products) have been produced in recent years, including the 30 m Global Land Cover (GlobeLand30) [26], [27], [28], the Finer Resolution Observation and Monitoring of Global Land Cover (FROM-GLC) [29], [30], [31], the Global Human Settlement Layer (GHSL) [32], [33], [34], the global artificial impervious areas (GAIA) [35], the global annual urban dynamics (GAUD) [36], the global impervious surface area (GISA) product [37], the updated global impervious surface area (GISA 2.0) [38], and the global land-cover product with fine classification system (GLC_FCS30) [39], [40]. The second-generation products were achieved by remote sensing images with a fine spatial resolution. In addition, these datasets with a high spatial resolution have smaller omission errors for impervious surface extraction in rural regions and low-density settlements.

GlobeLand30, as the first free and openly available 30-m global land-cover dataset, provides the earliest high spatial resolution ISA product for the years 2000, 2010, and 2020. The GHSL product is the first relatively long time-series (i.e., more than 30 year) global ISA product available at a 30-m spatial resolution, which depicts global changes in human settlement areas over the past 40 years [33]. Subsequently, the annual time-series global ISA products, e.g., GAIA, GAUD, GISA, and GISA 2.0, were successively generated to provide a reference for monitoring detailed urban, ecological, and environmental changes. The emergence of the second-generation global ISA products has also illustrated that relatively long time-series global ISA mapping has entered a new stage with the characteristics of high accuracy and high spatial resolution. More recently, the Joint Research Centre released two new versions of the GHSL product, i.e., a 2016 version with a resolution of 20 m and a 2018 version with a resolution of 10 m [32], [34]. In addition, Marconcini et al. [41] produced the World Settlement Footprint product with a 10-m resolution for the year of 2015, exploiting open-and-free Landsat 8 optical and Sentinel-1 radar satellite imagery. Furthermore, Esri developed a 10-m resolution global land-cover product with nine Level 1 classes for the year 2020 [42]. The above products have further increased the spatial resolution of the global ISA products, to 10 m and even higher spatial resolutions.

To date, global ISA mapping has evolved from static to dynamic (i.e., multiple periods), from coarse and medium spatial resolutions ($>$ 30 m) to high spatial resolutions ($\leq$ 30 m). The analysis and comparison of the global ISA datasets is of paramount importance, due to the increased amount of attention these products are generating. Although previous efforts have been made to analyze and compare the global ISA products [22], [23], [43], [44], these studies have mostly concentrated on area estimation and accuracy assessment of the static global ISA products (i.e., only one time series). A meta-analysis of the high-resolution global ISA products covering multiple periods, in regard to their data, samples and methods, is lacking in the current literature.

Thus, in this article, we target the existing high-resolution global ISA products with multiple time series (see Table I), and undertake a more in-depth review from three perspectives.

1) We provide an in-depth analysis of the differences between ISA products in terms of the data sources, sample collection, feature selection, and mapping methods, as well as the impact of these differences on the products.
2) By the use of a series of global multitemporal validation samples, the existing ISA products are evaluated separately at multitemporal and multispatial scales, with special attention paid to their performance in arid regions, rural regions, and different-level cities.
3) We investigate the differences and correlations of the high-resolution global ISA products through a consideration of the different scales, including global, continental, and grid scales. Furthermore, we explore the disagreement between datasets, and delve into the key points and problems of global ISA mapping.

We also list some recommendations for the future directions of high-resolution global ISA mapping.

II. High-Resolution Global ISA Mapping Frameworks

In this study, as shown in Table I, we analyzed eight public high spatial resolution global ISA products. This section provides a detailed review of the dataset information, including the data source, training samples, features, and methods.

A. Data Sources and Platform

High-resolution global ISA datasets are mainly derived from Landsat and Sentinel data, and supported by MODIS, nighttime light (NTL) data, Digital Elevation Model (DEM), and other ancillary data (see Table I). Landsat data, with the more than 40-year record, allow long-term ISA monitoring research (e.g., GISA 2.0, GISA, GAIA, GAUD, and GHSL) at a global scale. On the other hand, the ancillary data play a complementary role in global ISA mapping. For instance, NTL data can provide lighting information to reduce the false alarms caused by bright bare land and scattered vegetation, especially in arid regions, and MODIS normalized difference vegetation index (NDVI) data use the rich time-series information to describe the phenological characterization.

The storage and processing of huge amounts of remote sensing data is a challenge for mapping ISA at a global scale. In the early years, high-resolution global ISA mapping (e.g., GlobeLand30, FROM-GLC) was expensive in terms of the data acquisition and data processing. Since 2013, this situation has been greatly improved by the use of cloud computing platforms, e.g., GEE [27]. GEE offers a wide range of data sources (e.g., remote sensing images, ready-to-use data), creating an integrated model for data acquisition, processing, and analysis. As such, the advent of GEE has made it possible to quickly and efficiently map high-resolution ISA at a global scale. In particular, in recent years, a series of annual datasets e.g., GISA 2.0, GISA, GAIA and GAUD, covering a relatively long-term, have been developed.

The availability of remote sensing imagery is the basis for global ISA mapping. Based on the GEE platform, we counted

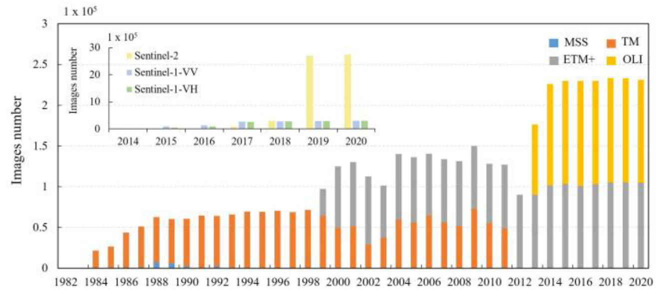

Fig. 1. Data availability from 1982 to 2020 based on GEE. Note: MSS, TM, ETM+ and OLI represent Multispectral. Scanner, Thematic Mapper, Enhanced Thematic Mapper Plus, and Operational Land Imager, respectively. Both VV and VH are single co-polarization. The former represents vertical transmit/vertical receive and the latter represents vertical transmit/horizontal receive.

the available data, with the cloud threshold set at 80%, for Landsat and Sentinel images from 1982 to 2020 (see Fig. 1). Overall, the annual observations have increased over the past three decades, and fewer Landsat images were available in the 1980s. To address this situation, some studies (e.g., GISA, GAIA) have supplemented the information with the help of images from adjacent time periods, to reduce the effect of missing data from the early years (e.g., the 1980s) [35], [37]. However, there are greater uncertainties in the early years in the long-term datasets (e.g., GISA 2.0, GISA, GAIA, GAUD, and GHSL) than in more recent years (e.g., after 2000). Sentinel images, with higher spatial resolution than Landsat, became available after 2015. Of these images, the Sentinel-1 images have shown great potential to support global ISA mapping, because of their all-day, all-weather characteristics. However, the short observation records of the Sentinel images signify that they cannot be used for long time-series ISA monitoring [46]. In order to ensure the quality and quantity of the imagery, some studies have employed remote sensing imagery from different sensors, but the inconsistency between satellite sensors is also an issue that needs to be considered [32], [47].

B. Training Sample Collection

Training samples are a crucial part of global high-resolution ISA mapping. There are the following three main ways to collect training samples in high-resolution global land-cover mapping:

1) field surveys [48];
2) visual interpretation based on high-resolution remote sensing imagery [49];
3) the use of open-source data (e.g., geographic information system (GIS) data, OpenStreetMap (OSM) data, settlement points data, existing land-cover datasets) [16].

Sample collection via field survey has the highest accuracy and reliability. However, this method is expensive and time-consuming, especially for large-scale and long-term land-cover mapping. In fact, visual interpretation or the use of open-source data is currently the most extensively used method of sample collection.

Visual interpretation is performed by interpreters to collect samples using high-resolution remote sensing imagery, such as Google Earth, Landsat, etc. Some studies have argued that the visual interpretation method tends to make the training samples less representative and comprehensive, because of the intervention of humans with limited domain knowledge [50]. In addition, collecting time-series training samples with a high quality for long time period land-cover mapping is still a challenge. Especially before 2000, there is greater uncertainty in the training samples obtained from visual interpretation, due to the unavailability of Google Earth images. Hence, some products, such as GISA and GAIA, refer to MODIS NDVI time-series data to improve the accuracy of multitemporal training samples.

On the other hand, through the use of open-source data, it is possible to automatically and efficiently select training samples, but these open-source data are often sourced from different organizations or institutions, so that the consistency and quality of the training samples can be not guaranteed. In addition, the training samples generated from the existing land-cover products are inevitably affected by classification errors.

The scale and representativeness of the training samples directly influences the mapping quality [51]. Insufficient, unrepresentative, and incorrect training samples introduce uncertainty and have a negative effect in the land-cover mapping procedure [11]. Generally, researchers prefer to use the stratified random sampling strategy to collect samples for global land-cover mapping [52], [53]. The obtained training samples are then secondarily checked to further ensure their quality. As it is difficult and challenging to check all the training samples at a global scale, researchers have usually randomly checked a proportion of the training samples. For example, Zhang et al. [40] selected 1% of the total training samples verify their representativeness and sensitivity.

Training sample collection is still a costly task in high-resolution global ISA mapping. Therefore, this calls for an automated or semi-automated method to collect accurate and sufficient samples [54]. Several studies have used mathematical morphology or distance detection methods to reduce the cost of sample collection and time-series sample update [55], [56], [57]. For example, Li and Xu [58] proposed a rapid method to extract training samples from multisource land-cover products, which effectively improved the reliability and accuracy of the samples; and Li and Xu [59] used a robust marginal distance detection method to automatically update 35 annual training samples for dynamic surface water mapping. More recently, Huang et al. [38] combined training samples from visual interpretation and automatic extraction to generate a new 30 m global ISA dataset (GISA 2.0), and the results indicated that this method further improves global ISA accuracy. Hence, these automatic and semi-automatic training sample collection methods are important references for high-resolution global ISA mapping.

C. Features of Global High-Resolution ISA Mapping

The features used in the existing high-resolution global ISA products can be categorized into topographic, spectral, synthetic aperture radar (SAR), and texture features (see Table II). Among the different features, spectral features are essential for extracting ISA information. Meanwhile, other features play a complementary role in global ISA mapping, and they contribute to further improving the accuracy of the datasets. Topographic features describe the elevation, slope, aspect of the land surface.

TABLE II
FEATURE INFORMATION OF THE EXISTING GLOBAL HIGH-RESOLUTION ISA MAPPING PRODUCTS

ISA product	Topography feature	Optical feature	SAR feature	Texture feature
GISA 2.0	Elevation, slope	Spectral bands and NDVI, MNDWI, NDBI (in their 20%, 50% and 80% percentiles) as well as their multi-temporal standard deviations	--	--
GISA	Elevation, slope	Spectral bands and NDVI, MNDWI, NDBI (in their 20%, 50% and 80% percentiles) as well as their multi-temporal standard deviations	--	--
GAIA	--	Spectral bands (such as SWIR), NDVI, MNDWI, NDVI (in their standard deviations, mean and anomaly)	Backscatter coefficients (i.e., VV and VH polarizations)	--
GAUD	--	Spectral bands (including blue, green, red, NIR, SWIR1, and SWIR2), NDVI, NDWI, and NDBI	--	--
GHSL	--	Spectral bands (including blue, green, red, NIR, and PAN), NDVI, etc.	--	Rotation-invariant and anisotropic contrast texture
GHSL 2016	Slope, aspect, and crest lines	--	Dual-polarization backscatter coefficients (VV and VH)	Texture (including the mean and standard deviation of the backscatter coefficients)
GHSL 2018	--	Spectral bands (including blue, green, red, and NIR)	--	--
GlobeLand30	--	Six spectral bands (such as red, NIR, SWIR, etc.), NDVI, and NDBI	--	Variance texture of the PAN band and NIR band
FROM-GLC 2010	--	Spectral bands (including blue, green, red, NIR, SWIR1 and SWIR2)	--	--
FROM-GLC 2015	--	Spectral bands (for example, blue, green)	--	--
FROM-GLC 2017	Elevation, slope, and aspect	Nine Landsat-8 image bands, NDVI, EVI, MNDWI, NDBI, NBI (in their 25%, 50% and 75% percentiles) as well as their standard deviations and mean	--	--
GLC_FCS30	Elevation, slope, and aspect	Spectral bands (including blue, green, red, NIR, SWIR1, and SWIR2), NDVI, NDBI, NDWI (in their 15% and 85%) as well as their mean and standard deviations	Backscatter coefficient (VV and VH polarizations)	Variance, dissimilarity and entropy textures of the NIR, VV, and VH

Note: Abbreviations: NDVI, normalized difference vegetation index; MNDWI, modified normalized difference water index; NDWI, normalized difference water index; NDBI, normalized difference built-up index; SWIR, shortwave infrared; NIR, near infrared; PAN, panchromatic; EVI, enhanced vegetation index; NBR, normalized burn ratio. Note: -- indicates that the corresponding feature is not used.

Owing to the unique characteristics of topographic features in mountainous and shaded areas, many studies (e.g., GISA 2.0, GISA, GHSL, FROM-GLC, and GLC_FCS30) have generated ISA products using topographic features at a global scale [30], [32], [37], [38], [40]. For instance, the GLC_FCS30 product considers elevation, slope, and aspect, calculated from the Shuttle Radar Topography Mission (SRTM) Advanced Spaceborne Thermal Emission and Reflection Radiometer DEM data, to help identify ISA. The GHSL product uses topographic features (including slope, aspect, and crest lines) to attenuate the confusion between the vertical structures of built-up areas and vertical land-cover classes (such as rock cliffs).

The spectral features [e.g., red, green, blue, near infrared (NIR), and shortwave infrared (SWIR) bands] have been found to be essential for mapping ISA datasets [60], [61]. In the 1990s, Ridd [62] decomposed the urban ecosystem into ISA and non-ISA (including vegetation, bare land, and water bodies). Hence, the essence of ISA mapping is to mask nonimpervious information. NDVI and EVI data are efficient ways to express vegetation information [63], but they are primarily acquired during the growing season, to increase the distinction between vegetation and other classes. Water bodies can be masked out by NDWI or MNDWI indices [64], [65]. Bare land can be extracted using the SWIR band, which can separate bare land from ISA in summer [66].The ISA information can also be identified using the normalized difference built-up index (NDBI), biophysical composition index, and built-up areas saliency index [67]. In addition, some studies, such as GISA 2.0, GISA, GAIA, FROM-GLC 2017, and GLC_FCS30, calculated the mean, percentage (e.g., 15%, 85%), and standard deviation of the spectral bands to obtain their temporal features [68], [69].

SAR features have the potential to mitigate the spectral similarity between ISA and other classes, because they canuseful information about the dielectric and geometric characteristics of ISA [70], [71], [72]. Among the existing high-resolution global datasets, GAIA uses backscatter coefficients to remove bare land from ISA in arid regions, and the GLC_FCS30 product fuses SAR and optical features to help with ISA recognition. However, SAR features cannot easily distinguish between mountainous areas with steep slopes and man-made facilities associated with water bodies (e.g., ships, drilling rigs, bridges). Compared to spectral features, SAR features have not been widely explored in ISA mapping, owing to the complexity of their interactions with the diverse ISA types [73], [74].

Texture features from high-resolution satellite imagery present the structure of ISA [11]. Several studies have pointed out the effectiveness of texture features for high-resolution global ISA mapping [75], [76]. For example, GHSL employs a string of textures, e.g., anisotropic contrast texture and backscatter texture, to improve the separability between ISA and the most confusing classes [33]; GlobeLand30 uses variance textures to extract ISA information in high heterogeneity areas; and GLC_FCS30 detects different ISA classes with the support of the variance, phase anisotropy, and entropy textures.

Several studies have analyzed the contribution of ISA mapping features [77], [78]. For example, Zhang et al. [72] compared optical and SAR features, and found that the optical features provided better ISA estimation results than the SAR features; Shao et al. [67] discovered that both optical features and single-polarized SAR features are useful for mapping global ISA, but the best mapping accuracy was achieved by fusing optical and SAR features; and Zhang et al. [40] ranked the contributions of the topographic-texture-optical-SAR features, and revealed that the VV and VH features are of the highest importance in most regions of the world, followed by the blue, green, red, and SWIR bands.

In summary, the optical and SAR features play a vital role in ISA mapping, but other features can be used to derive more ISA information. In order to achieve a high accuracy in global ISA mapping, the multifeature fusion approach is a good choice. Currently, the multifeature fusion approach is less commonly used in high-resolution global ISA mapping, however, it is able to achieve complementarity between features, reduce the classification uncertainties of spectral features, relieve the negative effects of spectral confusion (e.g., high-reflectance ISA with bare land, low reflectance ISA with shadows), and cope with the heterogeneous landscapes of ISA at a global scale. Therefore, the multifeature fusion approach provides a new possibility for high-resolution and high-quality global ISA mapping, and needs to be given more consideration in future research. At the same time, it will also be necessary to consider the computational cost of multiple features and the redundancy between features.

D. Mapping Methods

Studies of mapping ISA at regional, national, and global scales using satellite imagery were started more than four decades ago, and a wide range of methods have since been developed. Lu et al. [24] grouped the major ISA mapping methods into six categories [pixel-based, object-based, subpixel-based, spectral mixture analysis (SMA), regression analysis, and thresholding], according to the use of the remote sensing variables and techniques. In addition, Wang and Li [50] divided the ISA mapping methods into four categories, i.e., SMA, image classification, urban indices, and multisource data fusion, with respect to the characteristics and framework of the methods. Thus, researchers can choose the appropriate ISA mapping method by taking into account the data source, study purpose and application, study area scale, characteristics, etc. [11].

Random forest (RF), support vector machine (SVM), and decision tree classifiers are widely used, given the huge amount of data processing and computational cost in global ISA mapping. In addition, some studies have employed indices-based, threshold-based, regression-based, and deep learning methods to estimate ISA extent at a global scale (see Table I). In the time-series ISA mapping (e.g., GISA 2.0, GISA, and GAIA), the postprocessing methods are usually used for dealing with the classification errors of temporal-independent ISA maps [79]. The postprocessing methods often include the temporal consistency check and logical transition [80]. The temporal consistency check employs the temporal–spatial filter windows of different sizes, and aim to remove noise or misclassifications. The logical transition suppresses illogical conversion between land cover classes according to the transition rules, e.g., the ISA irreversibility rule [59], [81]. The postprocessing method is important for obtaining the temporally consistent ISA maps. The effectiveness of the postprocessing methods for generating more reliable ISA time-series information has been verified in a number of studies [82].

GlobeLand30 and FROM-GLC, as earlier high-resolution global ISA products, used multiple classifiers to complete the ISA mapping [26], [29], [45]. GlobeLand30 employed a combination of SVM and decision tree classifiers to cope with the complexity and diversity of the ISA environment. FROM-GLC 2010 employed SVM, RF, MLC, and J4.8 decision tree classifiers, and the results showed that the SVM classifier gave the highest mapping accuracy. However, the accuracy for the class of ISA was below 20%. This may be due to the fact that FROM-GLC 2010, as an attempt at global mapping, has shortcomings in the data selection, sample collection, and feature extraction.

The RF classifier is the most popular classifier in global high-resolution ISA mapping [83], [84]. This can be attributed to its following advantages:

1) robustness, in that the result is not easily affected by training sample errors;

2) stability, in that the mapping accuracy is less affected by the classifier parameters and input features;
3) the good tradeoff between mapping accuracy and computation time;
4) efficient handling of multidimensional multisource data [85], [86], [87], [88].

Notably, the locally adaptive RF method has been utilized in global ISA mapping, e.g., for GISA 2.0, GISA, and GLC_FCS30. The locally adaptive RF method partitions the mapping area into multiple regions, and then trains the classifier for each region using local training samples [89]. Studies have demonstrated that the locally adaptive RF approach increases the sensitivity to the quality of the training data and mitigates the deficiencies of migrating a single global classifier to other mapping regions [90], [91].

Deep learning has been applied in many remote sensing studies, due to its excellent performance in visual recognition, object detection, and semantic segmentation [92], [93], [94]. In recent years, deep learning has been put to use as a new tool for high-resolution global ISA mapping [95], [96]. For example, Corbane et al. [34] used a convolutional neural network (CNN) to develop the GHSL 2018 version, with a spatial resolution of 10 m; Liu et al. [97] adopted an intelligent mapping framework combining RF and machine learning to produce the first 30-m annual to seasonal global land-cover mapping product for 1985–2020; and Karra et al. [42] used deep learning models to train over 5 million Sentinel-2 artificial labels for developing global land-cover products at a 10-m resolution. The successful generation of the above products illustrates the great potential of deep learning methods for high-resolution large-scale ISA mapping, although its biggest impediment is the requirement for large numbers of training samples and large amount of computing power.

The mapping strategies also influence the global ISA mapping. The mapping strategies include: global and local strategies. The global strategies regard the globe as a whole, by constructing a single classification method using global training samples [40]. For example, FROM-GLC 2010 was generated using a global classifier with 91 433 training samples [29]. On the other hand, however, the local strategies split the globe into a number of regions, and a local classifier is trained with local training samples. Recently, researchers have indicated that the local strategies performed better than the global ones at balancing the data volume, reducing computation cost, and improving classification accuracy [89], [90]. Hence, in the recently developed global ISA products (e.g., GISA 2.0, GISA, GAIA, GAUD, and GLC_FCS30), the local classification strategies are preferred, by dividing the globe into amounts of grid tiles.

III. Accuracy Comparison Between Existing Global ISA Datasets

A. Collection of Test Samples

In this study, a series of independent test samples were collected to evaluate the accuracy of the existing high-resolution global ISA products (in Table I) over multiple temporal and multiple scales.

TABLE III
Global Human Settlement Points Statistics

Name	Year	Sample number
GRUMP	2000	39 401
	2001	13 321
	2002	3981
GeoNames	2010	2687
	2011	6194
	2012	21 552
	2013	7209
	2014	15 994
	2015	6828
	2016	12 530
	2017	26 854
	2018	17 809
	2019	14 345
Total	--	188 705

1) Manually Interpreted Samples: The manually interpreted samples (MI samples) were in 243 cities around the world. In order to evaluate the multiperiod accuracy of the high-resolution global ISA datasets, the MI samples covered nine sampling years (1978, 1985, 1990, 1995, 2000, 2005, 2010, 2015, and 2018), and were obtained with the assistance of high-resolution Google Earth images. For each sampling year, 27 cities were randomly selected across the world, in respect to their population and biomes, including seven large cities (population $>$ 5 million), 10 medium cities (1 million $<$ pop $<$ 5 million), and 10 small cities (population $<$ 1 million). For each city, the stratified random sampling method was used. According to the sampling strategy recommended by Olofsson et al. [52], the number of samples in each city was proportional to its area, and the number of samples per year was between 3000 and 6000. The sampling was conducted by experienced interpreters, and each interpreter was independent of the others in the sampling process. Additional interpreters were invited to check and correct the samples.

2) High-Resolution ZY3 Built-Up Area Samples (ZY3 Samples): Based on the high spatial resolution (3 m) multiview ZY3 remote sensing imagery, Liu et al. [98] established a built-up area dataset from 2012 to 2017 in 45 typical cities around the world. The ZY3 samples with a high spatial resolution and reliability were extracted from this built-up area dataset, and were used as test samples for assessing the global ISA dataset. Likewise, we used a stratified random sampling design. In addition, the interpreters carried out a secondary check of the ZY3 samples with reference to the high-resolution ZY3 imagery to ensure the correctness of the sample datasets. The spatial distribution of the MI samples and the ZY3 samples is shown in Fig. 2.

3) Global Settlement Points Data: We also validated the high-resolution global ISA datasets with the settlement points provided by the GRUMP [99] and GeoNames (http://download.geonames.org) (see Table III). These settlement points include the human habitations of different sizes around the world, and every point reflects the location of a city or town. As suggested by Gong et al. [100], we designed different buffers for every point, with diameters of 30, 100, 250, and 500 m, to represent the artificial impervious areas. As the number of settlement points varies between years (see Table III), the results are presented as

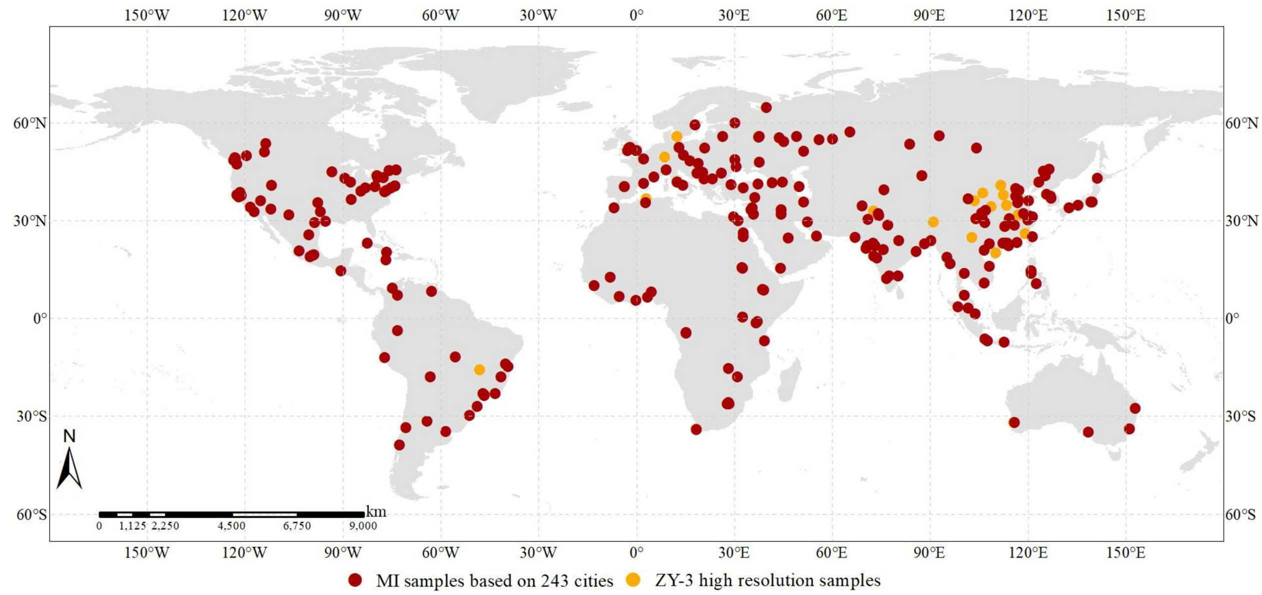

Fig. 2. Spatial distribution of the test samples.

the percentage of detected settlement points relative to the total number of settlement points.

B. Results

1) Accuracy Comparison: Table IV lists the test accuracies of the high spatial resolution global ISA products, as obtained from the MI samples and ZY3 samples. Focusing on the long time-series products (e.g., GISA 2.0, GISA, GAIA, GAUD, and GHSL), GISA 2.0 has the highest test accuracy, and its overall accuracy (OA) is 97.38% and 88.56% for the MI and ZY3 samples, respectively, followed by GISA (96.92%, 86.72%), GAUD (95.54%, 88.06%), GAIA (89.19%, 86.03%), and GHSL (94.37%, 83.72%). GISA 2.0 obtains the highest accuracy due to its concentration on the inconsistent regions of the existing global ISA products, and the mapping results in these regions were enhanced by adding manually interpreted samples [38]. It should be noted that GHSL provides only a few discontinuous time-series results. Consequently, the number of test samples for GHSL was 19 517 and 22 536 for the MI and ZY3 validation data, respectively, while the number of test samples for other long time-series products was 32 392 and 42 850.

Among short time-series products (e.g., GlobeLand30, FROM-GLC, and GLC_FCS30), GlobeLand30 has the highest accuracy, with an OA of 97.44% and 85.32% for MI and ZY test samples, respectively. The high accuracy of GlobeLand30 can be attributed to its use of the multiple-classifier mapping method (see Section II-D), which mitigated the spectral confusion of the different land-cover classes. In addition, the extensive consistency checking and manual interpretation guaranteed the quality of the GlobeLand30 product [46].

2) Multitemporal Accuracy At Global and Continental Levels: Fig. 3 shows the multitemporal OA of the high-resolution global ISA products obtained using the MI validation samples. As the percentage of ISA in Oceania is very small, we combined Oceania into Asia in this accuracy assessment. Overall, the OA displays an increasing trend during 1975–2020 at both global and continental scales. The trend in OA can be divided into two periods over the past 40 decades. Before 2000, the OA growth was dramatic, and the OA difference between various ISA products was significant; however, after 2000, the OA growth slowed, and the accuracy difference between different products gradually reduced. This pattern is mainly because of the improvement of the remote sensing image quality and quantity over time. For the long time-series datasets, the OA growth over time is more obvious.

The time-series OA curves also manifest different fluctuations at global and continental scales (see Fig. 3). At global scale, the OA curves of the ISA products are less fluctuated. Hence, the time-series OA curves of the continuous time-series products have small OA variance at global scale (see Fig. 4). Larger fluctuation of the OA curves is observed in Africa and South America, which shows that the ISA mapping results have more instabilities in these regions, and the time-series regularity and calibration need further enhancement. In contrast, the OA curves in Asia, Europe, and North America are relatively stable.

Among the long time-series products (i.e., GISA 2.0, GISA, GAIA, GAUD, and GHSL), GAUD presents the smallest OA variance at global scale (see Fig. 4). Hence, GAUD has the highest mapping stability, due to its use of temporal segmentation method [36]. GAIA has a large OA variance, indicating its poor mapping stability, especially in Asia, Europe, and Africa. In addition, the accuracy variance of GISA2.0 is also smaller, which demonstrates that it has advantages in both mapping accuracy and stability.

GlobeLand30, GLC_FCS30, and FROM-GLC are not discussed here, as they only provide a few discontinuous results. These datasets are also not considered in Section III-B, Section III-C, and Section III-D.

TABLE IV
HIGH-RESOLUTION ISA MAPPING ACCURACY OBTAINED FROM THE MI SAMPLES (LEFT COLUMN) AND ZY3 HIGH-RESOLUTION SAMPLES (RIGHT COLUMN) AT A GLOBAL SCALE

MI samples				ZY3 validation points			
GISA 2.0 (30 m)	ISA	NISA	UA (%)	GISA 2.0 (30m)	ISA	NISA	UA (%)
ISA	15 469	80	99.49	ISA	18 588	2066	90.00
NISA	768	16 075	95.44	NISA	2837	19 359	87.22
PU (%)	95.27	99.50	32 392	PU (%)	86.76	90.36	42 850
OA (%)	97.38	kappa	0.9476	OA (%)	88.56	kappa	0.7712
GISA (30 m)	ISA	NISA	UA (%)	GISA (30 m)	ISA	NISA	UA (%)
ISA	15 319	81	99.47	ISA	17 601	1867	90.41
NISA	918	16 992	94.60	NISA	3824	19 558	83.65
PU (%)	94.35	99.50	32 392	PU (%)	82.15	91.29	42 850
OA (%)	96.92	kappa	0.9383	OA (%)	86.72	kappa	0.7344
GAIA (30 m)	ISA	NISA	UA (%)	GAIA (30 m)	ISA	NISA	UA (%)
ISA	12 902	168	98.71	ISA	17 768	2331	88.40
NISA	3335	15 987	82.74	NISA	3657	19 094	83.93
PU (%)	79.46	98.96	32 392	PU (%)	82.93	89.12	42 850
OA (%)	89.19	kappa	0.78.38	OA (%)	86.03	kappa	0.7205
GAUD (30 m)	ISA	NISA	UA (%)	GAUD (30 m)	ISA	NISA	UA (%)
ISA	14 990	198	98.70	ISA	18 556	2248	89.19
NISA	1247	15 957	92.75	NISA	2869	19 177	86.99
PU (%)	92.32	98.77	32 392	PU (%)	86.61	89.51	42 850
OA (%)	95.54	kappa	0.9108	OA (%)	88.06	kappa	0.7612
GHSL (30 m-10 m)	ISA	NISA	UA (%)	GHSL (30 m-10 m)	ISA	NISA	UA (%)
ISA	8839	1[73]33	98.51	ISA	8548	1343	86.42
NISA	965	9580	90.85	NISA	2720	9925	78.49
PU (%)	90.16	98.63	19 517	PU (%)	75.86	88.08	22 536
OA (%)	94.37	kappa	0.8875	OA (%)	81.97	kappa	0.6394
GlobeLand30 (30 m)	ISA	NISA	UA (%)	GlobeLand30 (30 m)	ISA	NISA	UA (%)
ISA	4604	99	97.89	ISA	4323	933	82.25
NISA	144	4649	97.00	NISA	476	3866	89.04
PU (%)	96.97	97.91	9496	PU (%)	90.08	80.56	9598
OA (%)	97.44	kappa	0.9488	OA (%)	85.32	kappa	0.7064
FROM-GLC (30 m-10 m)	ISA	NISA	UA (%)	FROM-GLC (30 m-10 m)	ISA	NISA	UA (%)
ISA	6277	99	98.45	ISA	9441	1143	89.20
NISA	1791	7887	81.49	NISA	3908	12 206	75.75
PU (%)	77.80	98.76	16 054	PU (%)	70.72	91.44	26 698
OA (%)	88.22	kappa	0.76.48	OA (%)	81.08	kappa	0.6216
GLC_FCS30 (30 m)	ISA	NISA	UA (%)	GLC_FCS30 (30 m)	ISA	NISA	UA (%)
ISA	5323	263	95.29	ISA	10 869	1650	86.82
NISA	316	5294	94.37	NISA	2480	11 699	82.51
PU (%)	94.40	95.27	11 196	PU (%)	81.42	87.64	26 698
OA (%)	94.83	kappa	0.8966	OA (%)	84.53	kappa	0.6906

Note: OA: overall accuracy; UA: user accuracy; PA: product accuracy.

3) Accuracy At the City Level: We further tested the accuracy for the different-level cities. As illustrated in Fig. 5, the median OA for all the cities is greater than 89%. However, the large and medium cities show better results than the small ones, in terms of the maximum and median OA. Hence, more attention should be devoted to small cities in future work. In general, GAIA shows the largest variations for each city level. The GISA 2.0 and GISA achieve the high OA, but GISA shows large variance in the small cities. GAUD shows the smallest variation in all the city levels, but it has a lower accuracy in small cities. For GHSL, it can be seen that the variations of the accuracy become larger gradually from level 1 to level 3. Possible explanations include: 1) the definition of GHSL is focused more on urban areas, and 2) mapping rural ISA is more difficult than mapping urban ISA.

For the purpose of visual inspection, we randomly selected two large cities (Beijing and New York), two medium cities (Rome and Adelaide), and two small cities (Iquitos and Kindia). As seen from Fig. 6, the large and medium cities have more ISA with a concentrated and continuous distribution pattern, and these regions demonstrate a higher mapping accuracy and smaller differences between datasets. In contrast, the small cities, with low-density, fragmented ISA, have relatively lower mapping accuracy and larger differences between datasets. Moreover, we calculated the agreement extent of the global ISA products for the cities at different levels (the last row in Fig. 6), and found that large cities show a better agreement than medium and small cities.

Meanwhile, it is important to note that in the mapping results of the large and medium cities, their high agreement regions are mainly distributed in the urban centers. Thus, the regions surrounding the urban areas with discrete ISA objects still need to be given more attention for future global ISA mapping.

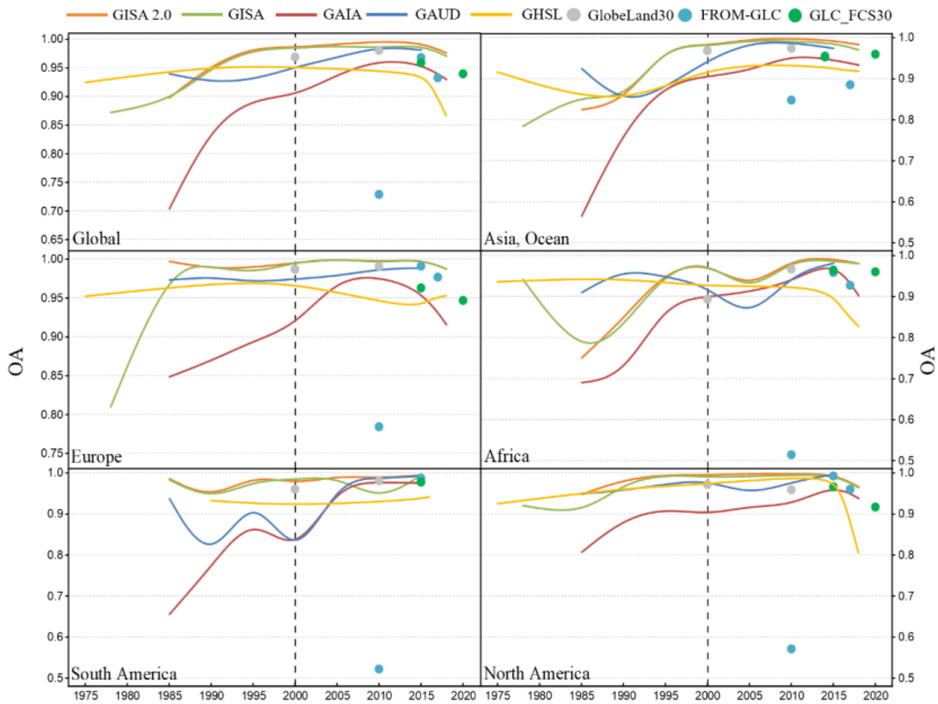

Fig. 3. Multiperiod accuracy of the high-resolution global ISA products at global and continental scales, where the accuracy was evaluated using the MI samples between 1978 and 2018.

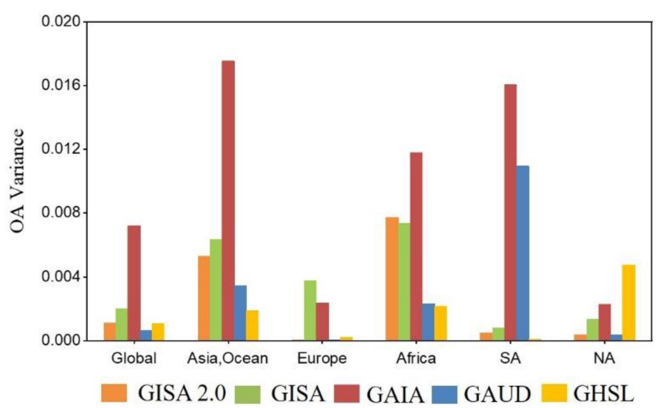

Fig. 4. Variance of multiperiod accuracy at global and continental scales. SA represents South America; NA represents North America.

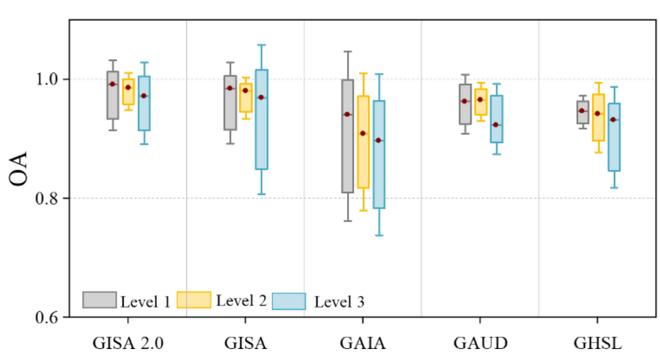

Fig. 5. Accuracy of the global ISA products at different city levels based on the MI validation samples. Level 1 represents a large city (pop > 5000 k), Level 2 represent a medium city (1000 k < pop < 5000 k), and Level 3 represents a small city (pop < 1000 k). The red dots represent the median OA values.

For these difficult regions, higher spatial resolution remote sensing imagery may be needed, to increase the identifiability of ISA.

C. Accuracy for Rural and Arid Regions

In arid regions, the ISA with high albedo can be confused with the surrounding bare land, due to their similar spectral properties, which usually leads to low classification accuracy in these regions [35], [100]. In rural regions, small and isolated impervious objects may result in omission and underestimation [101]. Therefore, we divided the mapping area into arid and nonarid regions, and urban and rural regions, respectively, according to global biome data and multitemporal global urban boundary data [35], [102]. We then assessed the accuracy of the long time-series global ISA products for arid and rural regions, using the MI samples. The spatial distribution of the samples is displayed in Figs. 15 and 16.

Table V illustrates that the accuracy in rural and arid regions is lower than the global accuracy (see Table IV). It is suggested that the mapping results for arid and rural regions are relatively poor. The rural and arid regions need to be paid more attention in future work. Specifically, the OA in arid regions in descending order is: GISA 2.0 (94.46%), GISA (90.78%), GHSL (84.96%), GAUD (84.79%), and GAIA (83.36%), and the OA in rural regions is: GISA 2.0 (91.31%), GISA (88.33%), GHSL (84.74%), GAUD (and 78.12%), and GAIA (72.10%).

In addition, the UA of the ISA products is generally higher than the PA in arid and rural regions, which is mainly because these regions have more non-ISA. Therefore, we used the F-score indicator to integrate PA and UA of the ISA products. The F-score also shows a similar situation: GISA 2.0> GISA > GHSL > GAUD > GAIA.

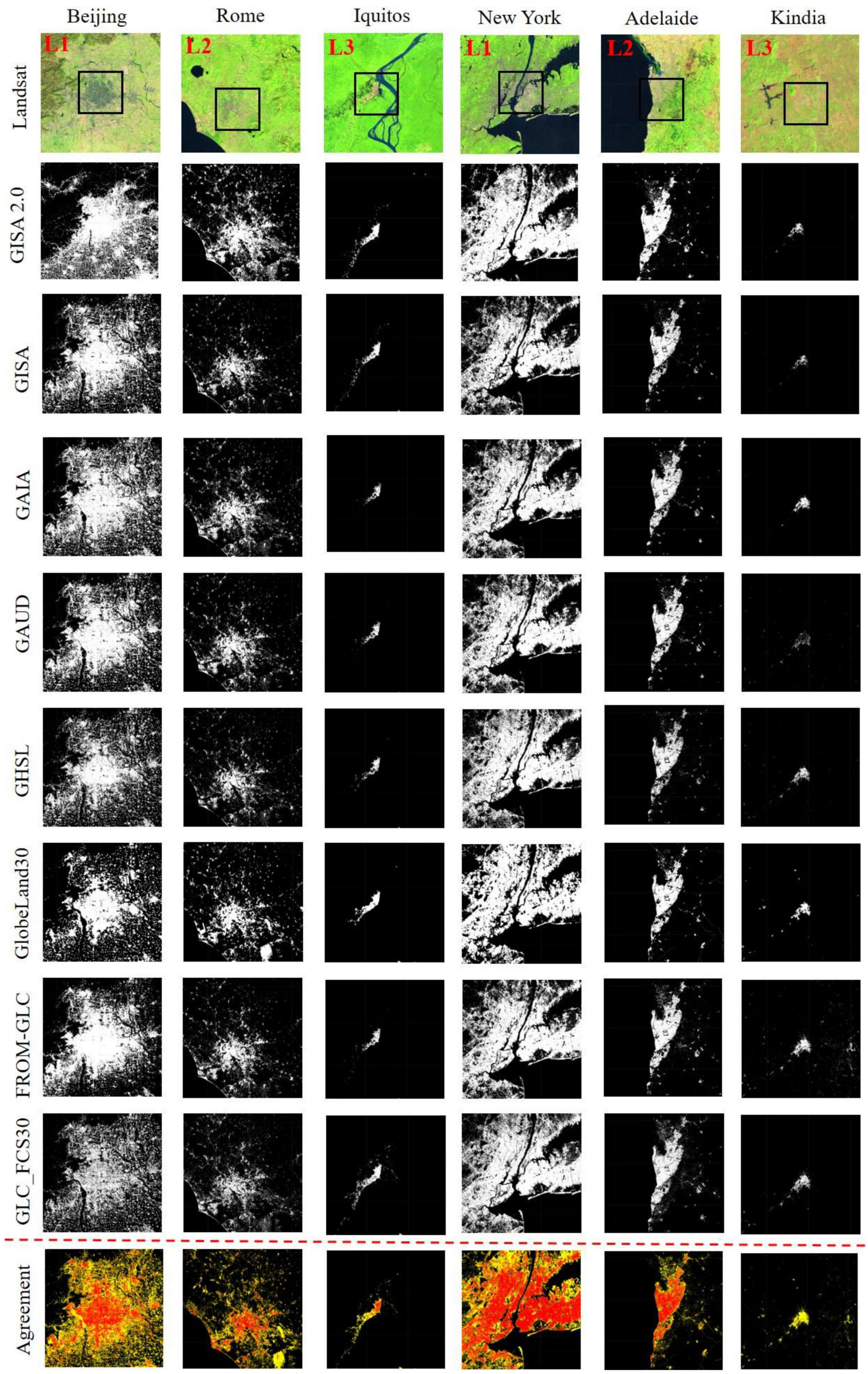

Fig. 6. Comparison of the global ISA products at different city levels. In the last row, red represents the mapping agreement area of the seven ISA products, and yellow represents the union of all the products. The patial extent of each subset is 100 km × 100 km. The Landsat image is a composite by the SWIR, NIR, and red bands. Level 1 represents a large city (pop > 5000 k), Level 2 represents a medium city (1000 k < pop < 5000 k), and Level 3 represents a small city (pop < 1000 k).

D. *Accuracy From Global Human Settlement Points*

Fig. 7 displays the accuracy of the long time-series datasets, assessed by the global human settlement points. In this case, GHSL shows the highest accuracy, since it targets built-up areas, i.e., houses and their surrounding neighborhoods [33], [34]. It should be kept in mind that GHSL has only four discontinuous periods, and hence, it uses much smaller settlement points than the other products in the test accuracy, which is a major reason for its highest accuracy. Of the long time-series ISA products (i.e., GISA 2.0, GISA, GAIA, and GAUD), the GHSL and GISA 2.0 are superior to other ones in most situations.

TABLE V
CONFUSION MATRICES FOR THE SEVEN ISA PRODUCTS AT A GLOBAL SCALE

Arid areas	OA (%)	Kappa	UA of ISA (%)	PA of ISA (%)	F-Score of ISA (%)
GISA 2.0	94.56	0.8913	99.12	89.93	94.30
GISA	90.78	0.8155	98.28	83.00	90.00
GAIA	83.36	0.6673	97.92	68.18	80.38
GAUD	84.79	0.6957	97.36	71.51	82.46
GHSL	84.96	0.6992	98.18	71.24	82.57
Rural areas	OA (%)	Kappa	UA of ISA (%)	PA of ISA (%)	F-Score of ISA (%)
GISA 2.0	91.31	0.8263	99.42	83.11	90.54
GISA	88.33	0.7666	98.94	77.49	86.91
GAIA	72.10	0.4420	97.66	45.29	61.88
GAUD	78.12	0.5623	98.06	57.37	72.39
GHSL	84.74	0.6948	98.01	70.92	82.29

Note: OA represents overall accuracy. UA represents user's accuracy. PA represents producer's accuracy.

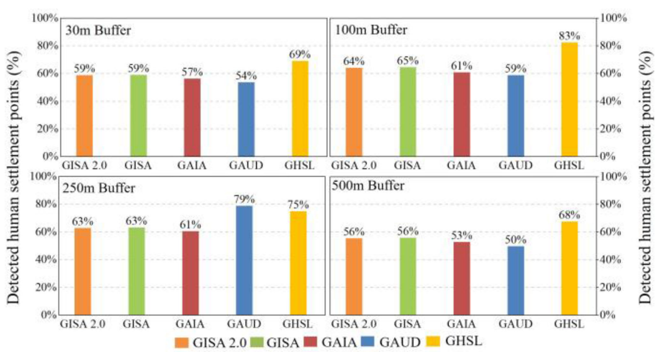

Fig. 7. Accuracy comparison for the ISA products based on global human settlement points.

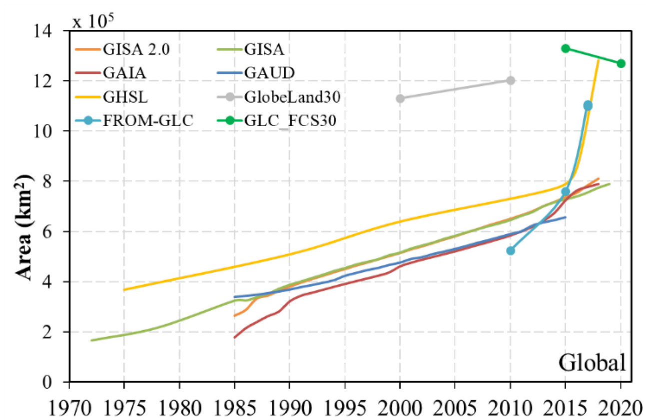

Fig. 8. Comparison of the ISA areas between different products at a global scale.

Buffer zones with different diameters affect the accuracy of the ISA products. When the buffer zone has a diameter of 100 or 250 m, the ISA products achieve the highest accuracy, and the accuracy of the ISA products is the lowest in a buffer with a 500-m diameter. This is because buffers with a small diameter include a high ISA proportion, so more settlement points can be recognized.

IV. Disagreement Between Existing Global ISA Products

A. Disagreement of ISA Area

The multitemporal area curves for the high spatial resolution ISA products at the global scale are shown in Fig. 8. Overall, most of the ISA products show reasonable temporal trends. However, the GLC_FCS30 and GHSL products exhibit anomalies, with regard to their area, in 2020 and 2016, respectively. This may be related to the fact that these products are made up of discontinuous time-series data, and thus lack time-series consistency corrections. Furthermore, the GHSL products for 2016 and 2018 are produced from different methods and data sources (see Table I), which could be a factor of the area anomalies. Other ISA products, such as GlobeLand30 and FROM-GLC, also suffer from similar problems to some extent. In contrast, the long time-series ISA products, such as GISA 2.0, GISA and GAUD, utilize postprocessing operations, e.g., the assumption that the transition from ISA to non-ISA is usually not likely, so that they possess more reasonable area growth trend.

According to Fig. 8, it is apparent that there are differences in the area curves for the existing high-resolution global ISA products. For instance, GlobeLand30, GLC_FCS30, and GHSL cover more ISA area at a global scale. While the ISA areas are very close between GISA 2.0 and GISA. Taking 2010 and 2015 as examples, we explored the spatial distribution and characteristics of these ISA products (see Fig. 9).

Fig. 9 indicates that GlobeLand30 and GLC_FCS30 cover more ISA area in Europe, South America, and North America. In particular, GlobeLand30 covers a significantly larger area than the other products in Europe. On the other hand, GLC_FCS30

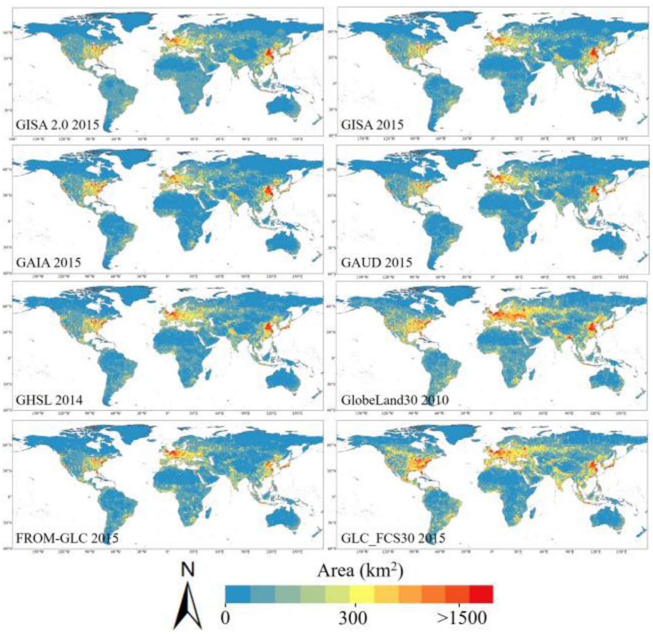

Fig. 9. Spatial distribution of the ISA products at a global scale. The impervious surface products are shown in a spatial grid of 100 km × 100 km, for convenience of visual inspection.

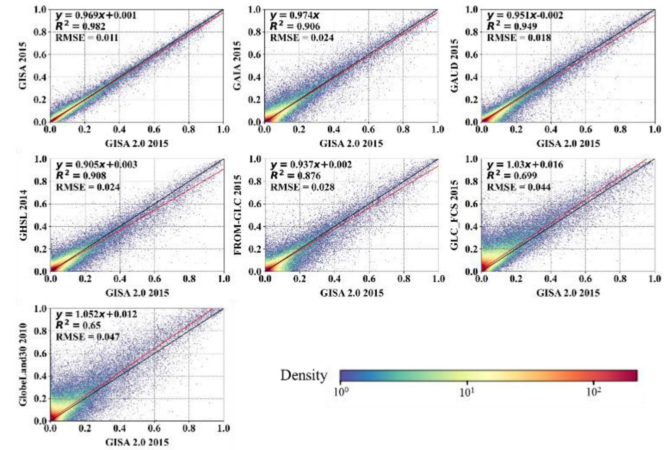

Fig. 10. Mapping area correlation between the ISA products at a global scale. The impervious surface products cover a spatial grid of 0.06° x 0.06°. The selected year of GlobeLand30 is 2010; the selected year of GISA, GAIA, GAUD, FROM-GLC, and GLC_FCS30 is 2015; the year of GHSL is 2014.

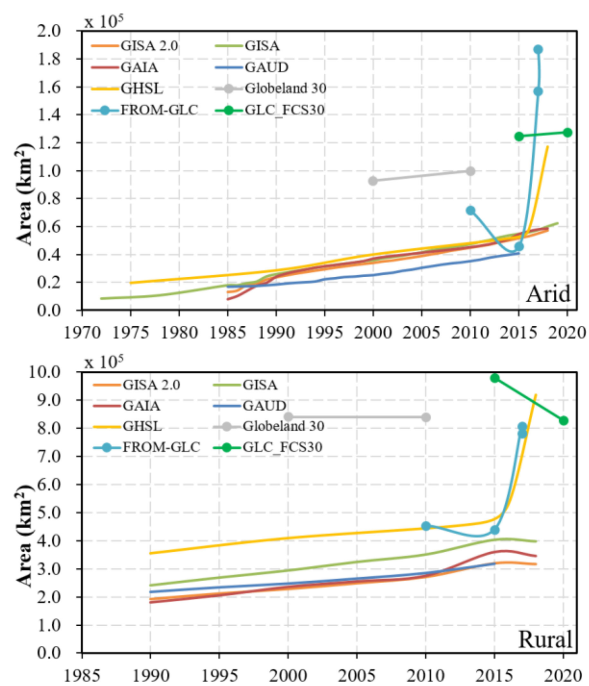

Fig. 11. Comparison of ISA area in arid and rural regions.

has a larger mapping extent in some regions, e.g., the United States and France, and a possible reason is that GLC_FCS30 has a better identification ability for small, fragmented ISA objects (e.g., villages and roads) [40]. In addition, the areas covered by GlobeLand30 and GLC_FCS30 are also relatively large in Africa and South America. In contrast, the ISA areas detected by FROM-GLC are small in all the continents.

As displayed in Fig. 9, for the long time-series products, GISA 2.0 and GISA have an equivalent area to GHSL in Asia, and covers a slightly larger area than GAIA and GAUD. Notably, GAIA extracts more impervious surfaces in China and India [35], due to the fact that it considers both urban and rural regions in the mapping results. GHSL has the largest ISA area in Europe, especially in England, France, and Germany. At a global scale, GISA 2.0, GISA, and GHSL show a larger area than GAIA and GAUD (see Fig. 8). A possible reason is that the GISA 2.0, GISA, and GHSL consider all of the global land area when extracting ISA, and they do not use an urban mask. Therefore, they have relatively less omission errors compared to GAUD [33], [37].

According to Fig. 3, GISA 2.0 shows better performances, compared to other datasets. Thus, using GISA as a reference, we investigated the correlation of the existing ISA products at a 0.06° spatial resolution (see Fig. 10). The results show that GISA 2.0 has the highest correlation with GISA ($R^2 = 0.982$, RMSE $= 0.011$), followed by GAUD ($R^2 = 0.949$, RMSE $= 0.018$), GHSL ($R^2 = 0.909$, RMSE $= 0.024$), GAIA ($R^2 = 0.906$, RMSE $= 0.024$), FROM-GLC ($R^2 = 0.876$, RMSE $= 0.028$), GLC_FCS30 ($R^2 = 0.699$, RMSE $= 0.044$), and GlobeLand30 ($R^2 = 0.592$, RMSE $= 0.049$). It can be said that the correlation between the long time-series products is high. This infers the necessity to consider temporal factors (e.g., temporal consistency checks, postprocessing constraints) when mapping time-series ISA products.

In addition, we further analyzed the multitemporal trends for the area of the ISA datasets in arid and rural regions (Fig. 11). The ISA area in arid regions only accounts for one-seventh of the total ISA. In contrast, the ISA area in rural regions accounts for more than half of the total. As shown in Fig. 11, GlobeLand30, GLC_FCS30, and FROM-GLC contain more ISA, in both arid and rural regions. In arid regions, GISA 2.0, GISA agrees with GAIA and GHSL, while GAUD shows a slightly smaller area. In rural regions, the curves of the high-resolution global products show similar patterns to those at the global scale (see Fig. 8), i.e., GHSL has a larger area than GISA, GAIA, and GAUD.

TABLE VI
GLOBAL ISA DATASETS USED IN SPATIAL DISAGREEMENT ANALYSIS FOR DIFFERENT YEARS

Year	ISA Products
1985	GISA2.0, GISA, GAIA, GAUD
1990	GISA2.0, GISA, GAIA, GAUD, GHSL
1995	GISA2.0, GISA, GAIA, GAUD
2000	GISA2.0, GISA, GAIA, GAUD, GHSL, GlobeLand30
2005	GISA2.0, GISA, GAIA, GAUD
2010	GISA2.0, GISA, GAIA, GAUD, GlobeLand30, FROM-GLC
2015	GISA2.0, GISA, GAIA, GAUD, GHSL, FROM-GLC, GLC_FCS30
2018	GISA2.0, GISA, GAIA, GHSL, FROM-GLC, GLC_FCS30

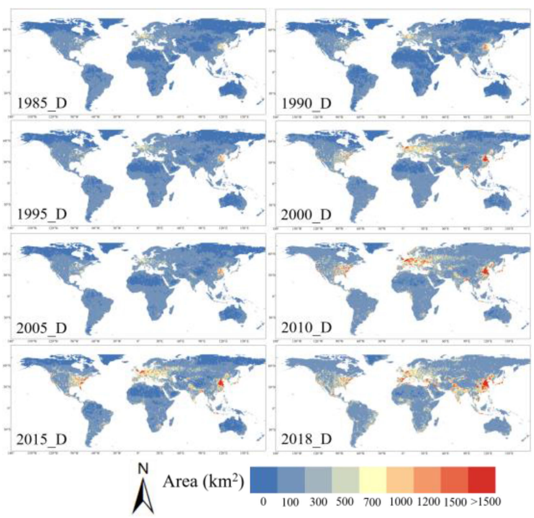

Fig. 12. Spatial distribution of the disagreement and agreement regions for the ISA products during 1985–2018. 1985_D represents the area of the disagreement regions within 100 km $\times$ 100 km grid in 1985.

B. Disagreement of ISA Spatial Distribution

Here we analyzed the disagreement between the high-resolution global ISA products at the global scale (see Fig. 13). Since the eight products range in spatial resolution from 10 to 30 m, we resampled these datasets to the 30-m resolution by the use of the nearest neighbor method. Table VI lists the global ISA datasets used in the disagreement analysis. In this article, the agreement regions are defined as the pixels identified as ISA in all the maps used. For instance, there are seven datasets considered in the disagreement analysis in 2015, and the pixels that was classified as ISA in seven datasets are considered as the agreement regions, otherwise the pixels are labeled as disagreement ones.

According to Table VI, we calculated the area of the disagreement pixels within 100 km $\times$ 100 km grid from 1985 to 2018 (see Fig. 12). We found that the higher disagreement mainly occurs in the ISA aggregation regions, e.g., eastern Asia, western Europe, and eastern North America, which should be focused on in future global ISA mapping. We also revealed that the disagreement is higher in 2000, 2010, 2015, and 2018. This may be related to the increase in the number of products (see Table VI). The release of GlobeLand30, GLC_FCS30, and FROM-GLC increased the disagreement between ISA products in these years.

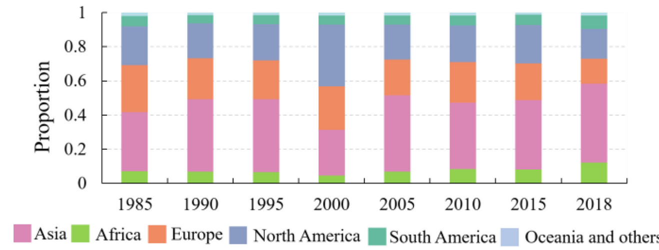

Fig. 13. Disagreement and agreement proportions for the ISA products at a continental scale during 1985–2018.

Moreover, we obtained the proportion of disagreement regions in different continents to the total disagreement regions of the global (see Fig. 13). During 1985–2018, the proportion of disagreement shows higher values in Asia, Europe, and North America than that in other continents. The total proportion of disagreement regions in these three continents (Asia, Europe, and North America) accounts for more than 78% of the total. Specifically, Asia has the highest agreement ($> 52\%$), which is slightly larger than that for North America and Europe.

As shown in Fig. 13, the high disagreement regions are mainly distributed in Asia, Europe, and North America (see Fig. 14). Fig. 14(a) represents low-density ISA regions (e.g., towns, roads). Due to the limitation of spatial resolution of remote sensing images and the number of training samples, larger omission errors were found in low-density regions [40]. Fig. 14(b) was covered by high-albedo bare land, where bare land generally exhibits similar spectral features with ISA, which leads to a large number of misclassifications. In Fig. 14(c) where the surface is covered by a large amount of vegetation, it can be seen that the mixed pixels still affect the mapping results. In general, the high disagreement regions are characterized by low density ISA and complex spatial distributions (e.g., the ISA was surrounded by high reflectance bare land or vegetation, where the background of ISA shows complex characteristics). In future work, the use of high spatial resolution remote sensing images, the fusion of multisource features (e.g., spectral-SAR features), and the increase of training samples in low-density ISA regions, may help to alleviate the misclassifications in the disagreement regions.

V. FUTURE RESEARCH DIRECTIONS

Based on the above analysis, comparison, and experiments, the following suggestions are made for future directions of global ISA mapping:

1) Cloud computing platforms: large-scale (national or global) land-cover mapping involves the acquisition, storage, and processing of huge amounts of data. Currently, cloud computing platforms (e.g., AWS, Microsoft Azure Cloud, PIE-Engine, GEE) offer new choices for rapid high spatial resolution ISA mapping. The AWS platform offers a range of machine learning and artificial intelligence tools. The Microsoft Azure Platform also provides a series of machine learning tools as well as construction, validation, displaying, and management for models and algorithms. Notably, the AWS and Microsoft Azure platforms

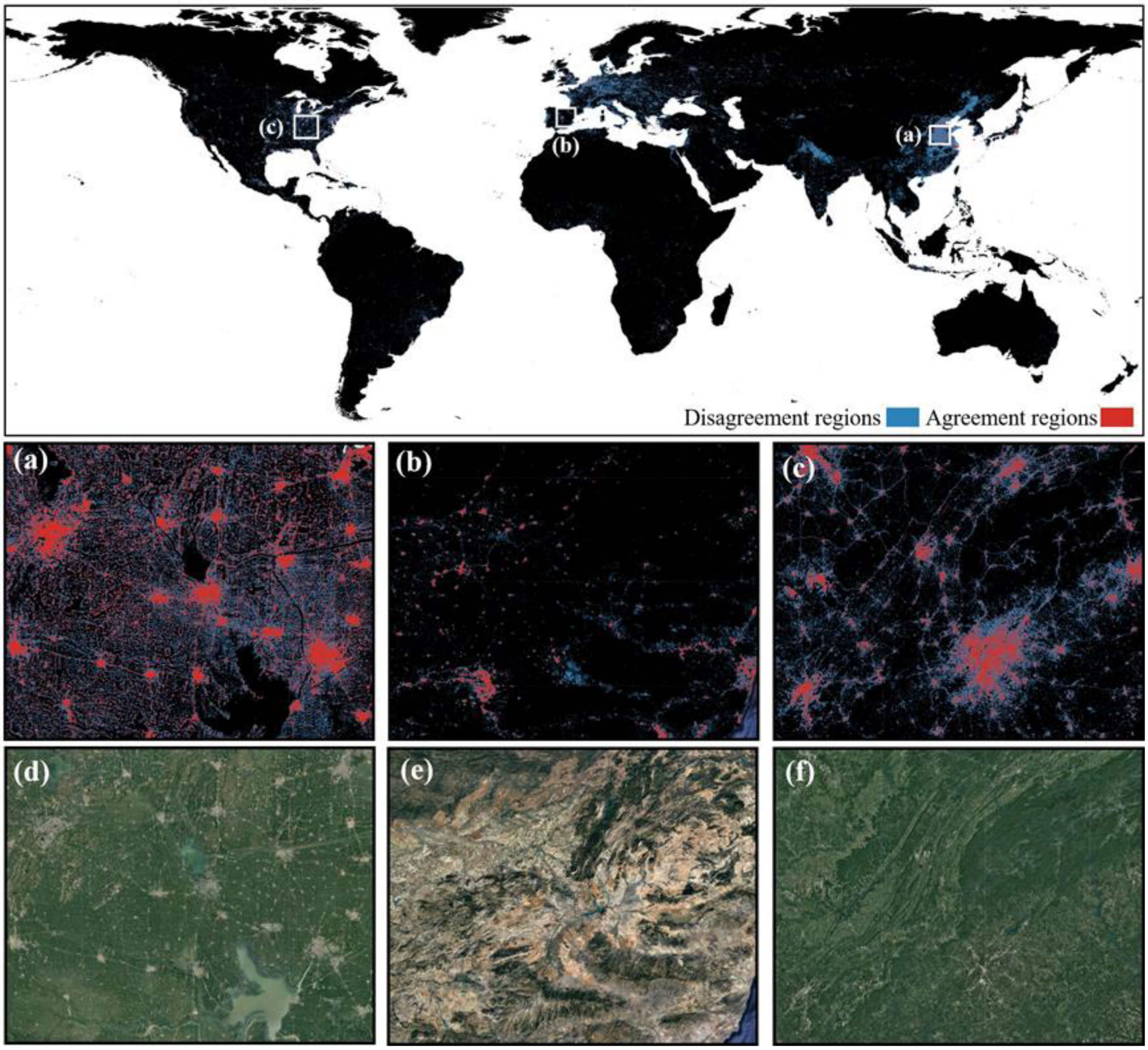

Fig. 14. Examples of disagreement regions. (a) Eastern China. (b) Spain. (c) Eastern United States. (d)–(f) represent Google Earth high-resolution images corresponding to (a)–(c), respectively.

are pay-as-you-go platforms, where the users can create their own data center [25], [28]. The PIE-Engine platform is a free cloud service platform developed in China, with abundant data (especially Gaofen and Fengyun satellite images) as well as processing and analysis capabilities [103]. However, to date, PIE-Engine has not been widely used worldwide. GEE is also a public platform that provides a wide range of remote sensing data and pay-as-you-go products. It was designed specifically for processing and analyzing geospatial datasets, and offered data storage, data analysis, machine learning tools, and mapping services [28], [104]. GEE has been successfully used to produce a large number of global land-cover products [27], [105]. Nevertheless, cloud computing platforms are still imperfect in many aspects, such as lack of convenient deep learning tools and computing resources.

2) Data: Global high spatial resolution ISA products still exhibit a large number of omission and commission problems. In particular, the ISA detection accuracy is poor in some areas, e.g., small urban, rural, and arid regions, owing to the high spatial heterogeneity and complexity of ISA in these regions. In future studies, higher resolution remote sensing imagery, such as Planet, WorldView, and ZY3 imagery, should have great potential for mapping these difficult regions, to mitigate the errors.

3) Method: The existing algorithms suffer from the classification errors, which are mainly caused by the spectral confusion between ISA and other similar land-cover classes, e.g., sandy land, bare land, and other bright objects. In order to solve this problem, multisource feature fusion methods could be applied [40], [48], [74]. In addition, deep learning algorithms, with their powerful feature expression capability, enable both low-level and high-level feature learning, which is beneficial for boosting the ISA classification performance in difficult regions. Currently, there have been a few cases to apply deep learning models to large-scale land-cover mapping [34], [42], [98]. This is a new and promising trend in high-resolution global ISA mapping.

4) Time-series modeling: One of the challenges in global ISA mapping is the reconstruction of long time-series land-cover classification results. The common methods include change detection [36] or ISA irreversibility constraints [37]. The change detection method inevitably leads to errors in the determination of the change breakpoint, while the irreversible constraint approach does not make full use of the multitemporal remote sensing image features. Therefore, how to make better use of time-series rules is an important direction in future global ISA mapping. Specifically, researchers could consider new time-series processing methods, such as long short-term memory networks [106], recurrent neural networks [107], and transformer architectures [108], [109].
5) Samples: Samples are a key factor in the ISA mapping, and influence the mapping accuracy. At the global scale, it is very difficult to collect adequate, correct, representative, and widely distributed samples. The current methods of sample collection include manual selection, refining from existing datasets, and selection from open-source data (e.g., OSM). However, these approaches are still labor intensive. In this context, the machine learning algorithms (e.g., weakly supervised and self-supervised learning algorithms), which can mine the characteristics of the data with small-size samples, may become future research directions [110], [111], [112].
6) Users: Production of global ISA products should be more demand oriented. Researchers in the ecological and environmental fields may require medium- or even coarse-resolution ISA datasets (300 m to 1 km), while very-high-resolution (e.g., finer than 5 m) ISA datasets may be required by regional or local users. Therefore, according to the needs of the users, global ISA products should involve multiple resolutions or scales, where very fine resolution ISA maps are generated when necessary.

VI. Conclusion

In recent years, high spatial resolution global ISA mapping has become a spotlight issue. Advances in remote sensing technology, methods, and data have motivated researchers to pay more attention to the high spatial resolution global ISA datasets. In this context, we conduct the first comprehensive and in-depth analysis of the existing high-resolution global multiple time-series ISA products.

The results show that, for long time-series maps (i.e., GISA 2.0, GISA, GAIA, GAUD, and GHSL), GISA 2.0 has the highest overall accuracy at global, arid and rural, and city scales. Therefore, GISA 2.0 can be served as a baseline of global ISA maps. Particularly, GAUD is more appropriate to reveal temporal change pattern of global ISA, due to its high temporal accuracy. In addition, GHSL pays attention on settlement points (see Section III-D), thus, it provides important reference to the study of human settlements.

We also obtained the disagreement regions for the existing global ISA products, which can be considered as the difficult and key regions for future ISA mapping. Last, we have provided an outlook on the future directions of global ISA mapping, in terms of cloud computing platforms, data sources, methods, time-series modeling, samples, and users.

Appendix

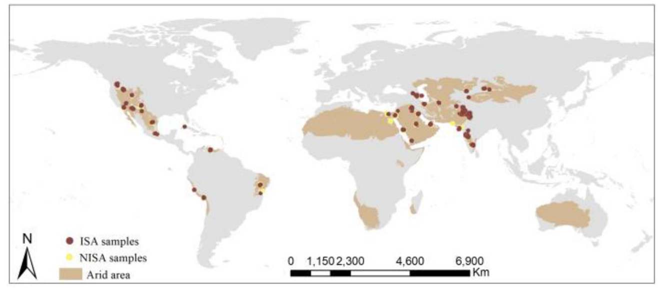

Fig. 15. Spatial distribution of the validation samples in arid regions.

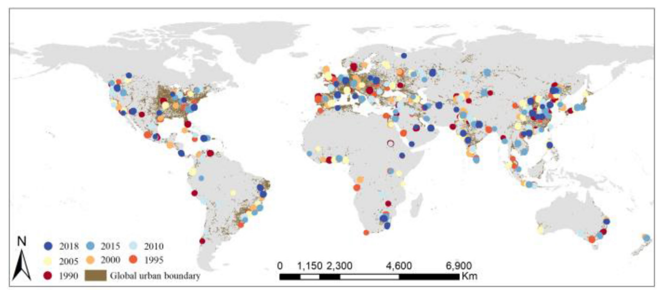

Fig. 16. Spatial distribution of the multiperiod validation samples in rural regions.

Acknowledgment

The authors would like to thank the editors and anonymous reviewers for their insightful and constructive suggestions, which significantly improved the quality of this article.

References

[1] E. Brabec, S. Schulte, and P. L. Richards, "Impervious surfaces and water quality: A review of current literature and its implications for watershed planning," *J. Plan. Literature*, vol. 16, no. 4, pp. 499–514, 2002, doi: 10.1177/088541202400903563.
[2] E. T. Slonecker, D. B. Jennings, and D. Garofalo, "Remote sensing of impervious surfaces: A review," *Remote Sens. Rev.*, vol. 20, no. 3, pp. 227–255, 2001, doi: 10.1080/02757250109532436.
[3] E. Wentz et al., "Supporting global environmental change research: A review of trends and knowledge gaps in urban remote sensing," *Remote Sens.*, vol. 6, no. 5, pp. 3879–3905, 2014, doi: 10.3390/rs6053879.
[4] F. Gao et al., "Mapping impervious surface expansion using medium-resolution satellite image time series: A case study in the Yangtze river delta, China," *Int. J. Remote Sens.*, vol. 33, no. 24, pp. 7609–7628, 2012, doi: 10.1080/01431161.2012.700424.
[5] P. Fu and Q. Weng, "A time series analysis of urbanization induced land use and land cover change and its impact on land surface temperature with landsat imagery," *Remote Sens. Environ.*, vol. 175, pp. 205–214, 2016, doi: 10.1016/j.rse.2015.12.040.
[6] C. L. Arnold and C. J. Gibbons, "Impervious surface coverage: The emergence of a key environmental indicator," *J. Amer. Plan. Assoc.*, vol. 62, no. 2, pp. 243–258, Jun. 1996, doi: 10.1080/01944369608975688.
[7] Y. Xie and Q. Weng, "Spatiotemporally enhancing time-series DMSP/OLS nighttime light imagery for assessing large-scale urban dynamics," *ISPRS J. Photogrammetry Remote Sens.*, vol. 128, pp. 1–15, 2017, doi: 10.1016/j.isprsjprs.2017.03.003.

[8] E. C. Stokes and K. C. Seto, "Characterizing and measuring urban landscapes for sustainability," *Environ. Res. Lett.*, vol. 14, no. 4, 2019, Art. no. 045002, doi: 10.1088/1748-9326/aafab8.

[9] J. A. Foley et al., "Global consequences of land use," *Science*, vol. 309, no. 5734, pp. 570–574, Jul. 2005, doi: 10.1126/science.1111772.

[10] Kiswanto, S. Tsuyuki, and Mardiany, and Sumaryono, "Completing yearly land cover maps for accurately describing annual changes of tropical landscapes," *Glob. Ecol. Conservation*, vol. 13, 2018, Art. no. e00384, doi: 10.1016/j.gecco.2018.e00384.

[11] Q. Weng, "Remote sensing of impervious surfaces in the urban areas: Requirements, methods, and trends," *Remote Sens. Environ.*, vol. 117, pp. 34–49, 2012, doi: 10.1016/j.rse.2011.02.030.

[12] H. L. D. Li and Z. Shao, "Review of impervious surface mapping using remote sensing technology and its application," *Geomatics Inf. Sci. Wuhan Univ.*, vol. 41, pp. 569–577, 2016, doi: 10.13203/j.whugis20160038.

[13] D. M. Danko, "The digital chart of the world project," *Photogrammetry Eng. Remote Sens.*, vol. 58, no. 8, 1992, Art. no. 8.

[14] K. Klein Goldewijk, A. Beusen, G. Van Drecht, and M. De Vos, "The HYDE 3.1 spatially explicit database of human-induced global land-use change over the past 12,000 years," *Glob. Ecol. Biogeography*, vol. 20, no. 1, pp. 73–86, 2011, doi: 10.1111/j.1466-8238.2010.00587.x.

[15] E. B. J. Dobson, P. Coleman, R. Durfee, and B. Worley, "LandScan: A global population database for estimating populations at risk," *Photogrammetry Eng. Remote Sens.*, vol. 66, pp. 849–857, 2000.

[16] D. L. Balk, U. Deichmann, G. Yetman, F. Pozzi, S. I. Hay, and A. Nelson, "Determining global population distribution: Methods, applications and data," in *Global Mapping of Infectious Diseases: Methods, Examples and Emerging Applications*, (Advances in Parasitology). Amsterdam, The Netherlands: Elsevier, 2006, pp. 119–156.

[17] E. Bartholomé and A. S. Belward, "GLC2000: A new approach to global land cover mapping from earth observation data," *Int. J. Remote Sens.*, vol. 26, no. 9, pp. 1959–1977, 2007, doi: 10.1080/01431160412331291297.

[18] A. Schneider, M. A. Friedl, and D. Potere, "Mapping global urban areas using MODIS 500-m data: New methods and datasets based on 'urban ecoregions'," *Remote Sens. Environ.*, vol. 114, no. 8, pp. 1733–1746, 2010, doi: 10.1016/j.rse.2010.03.003.

[19] M. A. Friedl et al., "MODIS collection 5 global land cover: Algorithm refinements and characterization of new datasets," *Remote Sens. Environ.*, vol. 114, no. 1, pp. 168–182, 2010, doi: 10.1016/j.rse.2009.08.016.

[20] O. Arino et al., "GlobCover: ESA service for global land cover from MERIS," in *Proc. IEEE Int. Geosci. Remote Sens. Symp.*, 2007, pp. 2412–2415.

[21] S. Bontemps et al., "Multi-year global land cover mapping at 300 m and characterization for climate modelling: Achievements of the land cover component of the ESA climate change initiative," in *Proc. Int. Arch. Photogrammetry, Remote Sens. Spatial Inf. Sci.*, 2015, pp. 323–328.

[22] M. Klotz, T. Kemper, C. Geiß, T. Esch, and H. Taubenböck, "How good is the map? A multi-scale cross-comparison framework for global settlement layers: Evidence from central Europe," *Remote Sens. Environ.*, vol. 178, pp. 191–212, 2016, doi: 10.1016/j.rse.2016.03.001.

[23] D. Potere and A. Schneider, "A critical look at representations of urban areas in global maps," *GeoJournal*, vol. 69, nos. 1/2, pp. 55–80, 2007, doi: 10.1007/s10708-007-9102-z.

[24] D. Lu, G. Li, W. Kuang, and E. Moran, "Methods to extract impervious surface areas from satellite images," *Int. J. Digit. Earth*, vol. 7, no. 2, pp. 93–112, 2014, doi: 10.1080/17538947.2013.866173.

[25] B. Wilder, "Cloud architecture patterns: Using microsoft azure," 2022. Accessed: May 19, 2022. [Online]. Available: https://docs.microsoft.com/en-us/azure/architecture/patterns/

[26] X. Chen et al., "Global mapping of artificial surfaces at 30-m resolution," *Sci. China Earth Sci.*, vol. 59, no. 12, pp. 2295–2306, 2016, doi: 10.1007/s11430-016-5291-y.

[27] N. Gorelick, M. Hancher, M. Dixon, S. Ilyushchenko, D. Thau, and R. Moore, "Google earth engine: Planetary-scale geospatial analysis for everyone," *Remote Sens. Environ.*, vol. 202, pp. 18–27, 2017, doi: 10.1016/j.rse.2017.06.031.

[28] K. R. Jackson et al., "Performance analysis of high performance computing applications on the amazon web services cloud," in *Proc. IEEE 2nd Int. Conf. Cloud Comput. Technol. Sci.*, 2010, pp. 159–168, doi: 10.1109/CloudCom.2010.69.

[29] P. Gong et al., "Finer resolution observation and monitoring of global land cover: First mapping results with landsat TM and ETM+ data," *Int. J. Remote Sens.*, vol. 34, no. 7, pp. 2607–2654, Apr. 2013, doi: 10.1080/01431161.2012.748992.

[30] P. Gong et al., "Stable classification with limited sample: Transferring a 30-m resolution sample set collected in 2015 to mapping 10-m resolution global land cover in 2017," *Sci. Bull.*, vol. 64, no. 6, pp. 370–373, 2019, doi: 10.1016/j.scib.2019.03.002.

[31] C. Li et al., "The first all-season sample set for mapping global land cover with landsat-8 data," *Sci. Bull.*, vol. 62, no. 7, pp. 508–515, 2017, doi: 10.1016/j.scib.2017.03.011.

[32] C. Corbane et al., "Big earth data analytics on sentinel-1 and landsat imagery in support to global human settlements mapping," *Big Earth Data*, vol. 1, nos. 1/2, pp. 118–144, 2017, doi: 10.1080/20964471.2017.1397899.

[33] C. Corbane et al., "Automated global delineation of human settlements from 40 years of landsat satellite data archives," *Big Earth Data*, vol. 3, no. 2, pp. 140–169, 2019, doi: 10.1080/20964471.2019.1625528.

[34] C. Corbane et al., "Convolutional neural networks for global human settlements mapping from sentinel-2 satellite imagery," *Neural Comput. Appl.*, vol. 33, no. 12, pp. 6697–6720, Jun. 2021, doi: 10.1007/s00521-020-05449-7.

[35] P. Gong et al., "Annual maps of global artificial impervious area (GAIA) between 1985 and 2018," *Remote Sens. Environ.*, vol. 236, 2020, Art. no. 111510, doi: 10.1016/j.rse.2019.111510.

[36] X. Liu et al., "High-spatiotemporal-resolution mapping of global urban change from 1985 to 2015," *Nature Sustain.*, vol. 3, no. 7, pp. 564–570, 2020, doi: 10.1038/s41893-020-0521-x.

[37] X. Huang, J. Li, J. Yang, Z. Zhang, D. Li, and X. Liu, "30 m global impervious surface area dynamics and urban expansion pattern observed by landsat satellites: From 1972 to 2019," *Sci. China Earth Sci.*, vol. 64, no. 11, pp. 1922–1933, Nov. 2021, doi: 10.1007/s11430-020-9797-9.

[38] X. Huang et al., "Toward accurate mapping of 30-m time-series global impervious surface area (GISA)," *Int. J. Appl. Earth Observ. GeoInf.*, vol. 109, May 2022, Art. no. 102787, doi: 10.1016/j.jag.2022.102787.

[39] X. Zhang, L. Liu, X. Chen, Y. Gao, S. Xie, and J. Mi, "GLC_FCS30: Global land-cover product with fine classification system at 30 m using time-series landsat imagery," *Earth Syst. Sci. Data*, vol. 13, no. 6, pp. 2753–2776, 2021, doi: 10.5194/essd-13-2753-2021.

[40] X. Zhang et al., "Development of a global 30 m impervious surface map using multisource and multitemporal remote sensing datasets with the google earth engine platform," *Earth Syst. Sci. Data*, vol. 12, no. 3, pp. 1625–1648, 2020, doi: 10.5194/essd-12-1625-2020.

[41] M. Marconcini et al., "Outlining where humans live, the world settlement footprint 2015," *Sci. Data*, vol. 7, no. 1, Jul. 2020, Art. no. 242, doi: 10.1038/s41597-020-00580-5.

[42] K. Karra, C. Kontgis, Z. Statman-Weil, J. C. Mazzariello, M. Mathis, and S. P. Brumby, "Global land use/land cover with sentinel 2 and deep learning," in *Proc. IEEE Int. Geosci. Remote Sens. Symp.*, 2021, pp. 4704–4707.

[43] D. Potere, A. Schneider, S. Angel, and D. L. Civco, "Mapping urban areas on a global scale: Which of the eight maps now available is more accurate?," *Int. J. Remote Sens.*, vol. 30, no. 24, pp. 6531–6558, 2009, doi: 10.1080/01431160903121134.

[44] A. J. Tatem, A. M. Noor, and S. I. Hay, "Assessing the accuracy of satellite derived global and national urban maps in Kenya," *Remote Sens. Environ.*, vol. 96, no. 1, pp. 87–97, May 2005, doi: 10.1016/j.rse.2005.02.001.

[45] J. Chen et al., "Global land cover mapping at 30m resolution: A POK-based operational approach," *ISPRS J. Photogrammetry Remote Sens.*, vol. 103, pp. 7–27, 2015, doi: 10.1016/j.isprsjprs.2014.09.002.

[46] L. Liu, X. Zhang, Y. Gao, X. Chen, X. Shuai, and J. Mi, "Finer-Resolution mapping of global land cover: Recent developments, consistency analysis, and prospects," *J. Remote Sens.*, vol. 2021, pp. 1–38, 2021, doi: 10.34133/2021/5289697.

[47] D. P. Roy et al., "Characterization of landsat-7 to landsat-8 reflective wavelength and normalized difference vegetation index continuity," *Remote Sens. Environ.*, vol. 185, no. 1, pp. 57–70, Jan. 2016, doi: 10.1016/j.rse.2015.12.024.

[48] A. J. Oliphant et al., "Mapping cropland extent of southeast and northeast Asia using multi-year time-series landsat 30-m data using a random forest classifier on the google earth engine cloud," *Int. J. Appl. Earth Observ. Geoinf.*, vol. 81, pp. 110–124, 2019, doi: 10.1016/j.jag.2018.11.014.

[49] L. Yu and P. Gong, "Google earth as a virtual globe tool for earth science applications at the global scale: Progress and perspectives," *Int. J. Remote Sens.*, vol. 33, no. 12, pp. 3966–3986, 2011, doi: 10.1080/01431161.2011.636081.

[50] Y. Wang and M. Li, "Urban impervious surface detection from remote sensing images: A review of the methods and challenges," *IEEE Geosci. Remote Sens. Mag.*, vol. 7, no. 3, pp. 64–93, Sep. 2019.

[51] D. Lu and Q. Weng, "A survey of image classification methods and techniques for improving classification performance," *Int. J. Remote Sens.*, vol. 28, no. 5, pp. 823–870, 2007, doi: 10.1080/01431160600746456.
[52] P. Olofsson, G. M. Foody, M. Herold, S. V. Stehman, C. E. Woodcock, and M. A. Wulder, "Good practices for estimating area and assessing accuracy of land change," *Remote Sens. Environ.*, vol. 148, pp. 42–57, 2014, doi: 10.1016/j.rse.2014.02.015.
[53] Z. Zhu et al., "Optimizing selection of training and auxiliary data for operational land cover classification for the LCMAP initiative," *ISPRS J. Photogrammetry Remote Sens.*, vol. 122, pp. 206–221, Dec. 2016, doi: 10.1016/j.isprsjprs.2016.11.004.
[54] Y. Ban, P. Gong, and C. Giri, "Global land cover mapping using earth observation satellite data: Recent progresses and challenges," *ISPRS J. Photogrammetry Remote Sens.*, vol. 103, pp. 1–6, 2015, doi: 10.1016/j.isprsjprs.2015.01.001.
[55] W. Huang et al., "Automated extraction of surface water extent from sentinel-1 data," *Remote Sens.*, vol. 10, no. 5, 2018, Art. no. 797, doi: 10.3390/rs10050797.
[56] K. Jia, S. Liang, X. Wei, L. Zhang, Y. Yao, and S. Gao, "Automatic land-cover update approach integrating iterative training sample selection and a markov random field model," *Remote Sens. Lett.*, vol. 5, no. 2, pp. 148–156, 2014, doi: 10.1080/2150704x.2014.889862.
[57] K. Wessels et al., "Rapid land cover map updates using change detection and robust random forest classifiers," *Remote Sens.*, vol. 8, no. 11, 2016, Art. no. 888, doi: 10.3390/rs8110888.
[58] K. Li and E. Xu, "Cropland data fusion and correction using spatial analysis techniques and the google earth engine," *GISci. Remote Sens.*, vol. 57, no. 8, pp. 1026–1045, 2020, doi: 10.1080/15481603.2020.1841489.
[59] K. Li and E. Xu, "High-accuracy continuous mapping of surface water dynamics using automatic update of training samples and temporal consistency modification based on google earth engine: A case study from Huizhou, China," *ISPRS J. Photogrammetry Remote Sens.*, vol. 179, pp. 66–80, 2021, doi: 10.1016/j.isprsjprs.2021.07.009.
[60] E. Ben-Dor, N. Levin, and H. Saaroni, "A spectral based recognition of the urban environment using the visible and near-infrared spectral region (0.4-1.1 μm). A case study over tel-aviv, Israel," *Int. J. Remote Sens.*, vol. 22, no. 11, pp. 2193–2218, 2010, doi: 10.1080/01431160117759.
[61] M. Herold, X. Liu, and K. C. Clarke, "Spatial metrics and image texture for mapping urban land use," *Photogrammetric Eng. Remote Sens.*, vol. 69, no. 9, pp. 991–1001, 2003, doi: 10.14358/pers.69.9.991.
[62] M. K. Ridd, "Exploring a V-I-S (vegetation-impervious surface-soil) model for urban ecosystem analysis through remote sensing: Comparative anatomy for cities†," *Int. J. Remote Sens.*, vol. 16, no. 12, pp. 2165–2185, 2007, doi: 10.1080/01431169508954549.
[63] C. J. Tucker, "Red and photographic infrared linear combinations for monitoring vegetation," *Remote Sens. Environ.*, vol. 8, no. 2, pp. 127–150, May 1979, doi: 10.1016/0034-4257(79)90013-0.
[64] S. K. McFeeters, "The use of the normalized difference water index (NDWI) in the delineation of open water features," *Int. J. Remote Sens.*, vol. 17, no. 7, pp. 1425–1432, 2007, doi: 10.1080/01431169608948714.
[65] H. Xu, "Modification of normalised difference water index (NDWI) to enhance open water features in remotely sensed imagery," *Int. J. Remote Sens.*, vol. 27, no. 14, pp. 3025–3033, Jul. 2006, doi: 10.1080/01431160600589179.
[66] X. Li and P. Gong, "An 'exclusion-inclusion' framework for extracting human settlements in rapidly developing regions of China from landsat images," *Remote Sens. Environ.*, vol. 186, pp. 286–296, 2016, doi: 10.1016/j.rse.2016.08.029.
[67] Z. Shao, H. Fu, P. Fu, and L. Yin, "Mapping urban impervious surface by fusing optical and SAR data at the decision level," *Remote Sens.*, vol. 8, no. 11, 2016, Art. no. 945, doi: 10.3390/rs8110945.
[68] D. Sulla-Menashe, J. M. Gray, S. P. Abercrombie, and M. A. Friedl, "Hierarchical mapping of annual global land cover 2001 to present: The MODIS collection 6 land cover product," *Remote Sens. Environ.*, vol. 222, pp. 183–194, 2019, doi: 10.1016/j.rse.2018.12.013.
[69] X. Li, Y. Zhou, Z. Zhu, and W. Cao, "A national dataset of 30 m annual urban extent dynamics (1985–2015) in the conterminous United States," *Earth Syst. Sci. Data*, vol. 12, no. 1, pp. 357–371, 2020, doi: 10.5194/essd-12-357-2020.
[70] Y. Zhang, H. Zhang, and H. Lin, "Improving the impervious surface estimation with combined use of optical and SAR remote sensing images," *Remote Sens. Environ.*, vol. 141, pp. 155–167, 2014, doi: 10.1016/j.rse.2013.10.028.
[71] H. Zhang, H. Lin, and Y. Wang, "A new scheme for urban impervious surface classification from SAR images," *ISPRS J. Photogrammetry Remote Sens.*, vol. 139, pp. 103–118, 2018, doi: 10.1016/j.isprsjprs.2018.03.007.
[72] H. Zhang, Y. Zhang, and H. Lin, "A comparison study of impervious surfaces estimation using optical and SAR remote sensing images," *Int. J. Appl. Earth Observ. GeoInf.*, vol. 18, pp. 148–156, 2012, doi: 10.1016/j.jag.2011.12.015.
[73] Y. Ban, A. Jacob, and P. Gamba, "Spaceborne SAR data for global urban mapping at 30m resolution using a robust urban extractor," *ISPRS J. Photogrammetry Remote Sens.*, vol. 103, pp. 28–37, May 2015, doi: 10.1016/j.isprsjprs.2014.08.004.
[74] Z. Sun, R. Xu, W. Du, L. Wang, and D. Lu, "High-Resolution urban land mapping in China from sentinel 1A/2 imagery based on google earth engine," *Remote Sens.*, vol. 11, no. 7, 2019, Art. no. 752, doi: 10.3390/rs11070752.
[75] T. Esch et al., "Urban footprint processor—Fully automated processing chain generating settlement masks from global data of the TanDEM-X mission," *IEEE Geosci. Remote Sens. Lett.*, vol. 10, no. 6, pp. 1617–1621, Nov. 2013.
[76] P. Gamba, M. Aldrighi, and M. Stasolla, "Robust extraction of urban area extents in HR and VHR SAR images," *IEEE J. Sel. Topics Appl. Earth Observ. Remote Sens.*, vol. 4, no. 1, pp. 27–34, Mar. 2011.
[77] H. Guan, J. Li, M. Chapman, F. Deng, Z. Ji, and X. Yang, "Integration of orthoimagery and lidar data for object-based urban thematic mapping using random forests," *Int. J. Remote Sens.*, vol. 34, no. 14, pp. 5166–5186, 2013, doi: 10.1080/01431161.2013.788261.
[78] Y. Lin, H. Zhang, H. Lin, P. E. Gamba, and X. Liu, "Incorporating synthetic aperture radar and optical images to investigate the annual dynamics of anthropogenic impervious surface at large scale," *Remote Sens. Environ.*, vol. 242, 2020, Art. no. 111757, doi: 10.1016/j.rse.2020.111757.
[79] N. Wang, W. Li, R. Tao, and Q. Du, "Graph-based block-level urban change detection using sentinel-2 time series," *Remote Sens. Environ.*, vol. 274, 2022, Art. no. 112993, doi: 10.1016/j.rse.2022.112993.
[80] S. Xie, L. Liu, X. Zhang, and J. Yang, "Mapping the annual dynamics of land cover in Beijing from 2001 to 2020 using landsat dense time series stack," *ISPRS J. Photogrammetry Remote Sens.*, vol. 185, pp. 201–218, 2022, doi: 10.1016/j.isprsjprs.2022.01.014.
[81] J. Yang and X. Huang, "The 30 m annual land cover dataset and its dynamics in China from 1990 to 2019," *Earth Syst. Sci. Data*, vol. 13, no. 8, pp. 3907–3925, 2021, doi: 10.5194/essd-13-3907-2021.
[82] X. Li, P. Gong, and L. Liang, "A 30-year (1984–2013) record of annual urban dynamics of Beijing city derived from landsat data," *Remote Sens. Environ.*, vol. 166, pp. 78–90, 2015, doi: 10.1016/j.rse.2015.06.007.
[83] A. Ghosh and P. K. Joshi, "A comparison of selected classification algorithms for mapping bamboo patches in lower gangetic plains using very high resolution worldview 2 imagery," *Int. J. Appl. Earth Observ. GeoInf.*, vol. 26, pp. 298–311, 2014, doi: 10.1016/j.jag.2013.08.011.
[84] D. Chutia, D. K. Bhattacharyya, K. K. Sarma, R. Kalita, and S. Sudhakar, "Hyperspectral remote sensing classifications: A perspective survey," *Trans. GIS*, vol. 20, no. 4, pp. 463–490, 2016, doi: 10.1111/tgis.12164.
[85] M. Belgiu and L. Drăguţ, "Random forest in remote sensing: A review of applications and future directions," *ISPRS J. Photogrammetry Remote Sens.*, vol. 114, pp. 24–31, 2016, doi: 10.1016/j.isprsjprs.2016.01.011.
[86] V. F. Rodriguez-Galiano, B. Ghimire, J. Rogan, M. Chica-Olmo, and J. P. Rigol-Sanchez, "An assessment of the effectiveness of a random forest classifier for land-cover classification," *ISPRS J. Photogrammetry Remote Sens.*, vol. 67, pp. 93–104, 2012, doi: 10.1016/j.isprsjprs.2011.11.002.
[87] C. Pelletier, S. Valero, J. Inglada, N. Champion, and G. Dedieu, "Assessing the robustness of random forests to map land cover with high resolution satellite image time series over large areas," *Remote Sens. Environ.*, vol. 187, pp. 156–168, 2016, doi: 10.1016/j.rse.2016.10.010.
[88] P. O. Gislason, J. A. Benediktsson, and J. R. Sveinsson, "Random forests for land cover classification," *Pattern Recognit. Lett.*, vol. 27, no. 4, pp. 294–300, 2006, doi: 10.1016/j.patrec.2005.08.011.
[89] H. K. Zhang and D. P. Roy, "Using the 500 m MODIS land cover product to derive a consistent continental scale 30 m landsat land cover classification," *Remote Sens. Environ.*, vol. 197, pp. 15–34, 2017, doi: 10.1016/j.rse.2017.05.024.
[90] J. Radoux, C. Lamarche, E. Van Bogaert, S. Bontemps, C. Brockmann, and P. Defourny, "Automated training sample extraction for global land cover mapping," *Remote Sens.*, vol. 6, no. 5, pp. 3965–3987, 2014, doi: 10.3390/rs6053965.
[91] A. Juel, G. B. Groom, J.-C. Svenning, and R. Ejrnæs, "Spatial application of random forest models for fine-scale coastal vegetation classification using object based analysis of aerial orthophoto and DEM data," *Int. J. Appl. Earth Observ. GeoInf.*, vol. 42, pp. 106–114, 2015, doi: 10.1016/j.jag.2015.05.008.

[92] N. Audebert et al., "Deep learning for urban remote sensing," in *Proc. IEEE Joint Urban Remote Sens. Event*, Mar. 2017, pp. 1–4, doi: 10.1109/JURSE.2017.7924536.
[93] O. A. B. Penatti, K. Nogueira, and J. A. dos Santos, "Do deep features generalize from everyday objects to remote sensing and aerial scenes domains?," in *Proc. IEEE Conf. Comput. Vis. Pattern Recognit. Workshops*, 2015, pp. 44–51.
[94] V. Mnih and G. E. Hinton, "Learning to detect roads in high-resolution aerial images," in *Proc. Eur. Conf. Comput. Vis.*, 2010, pp. 210–223.
[95] J. Yang, L. Ji, X. Geng, X. Yang, and Y. Zhao, "Building detection in high spatial resolution remote sensing imagery with the U-Rotation detection network," *Int. J. Remote Sens.*, vol. 40, no. 15, pp. 6036–6058, 2019, doi: 10.1080/01431161.2019.1587200.
[96] Y. Xu, L. Wu, Z. Xie, and Z. Chen, "Building extraction in very high resolution remote sensing imagery using deep learning and guided filters," *Remote Sens.*, vol. 10, no. 1, 2018, Art. no. 144, doi: 10.3390/rs10010144.
[97] H. Liu, P. Gong, J. Wang, X. Wang, G. Ning, and B. Xu, "Production of global daily seamless data cubes and quantification of global land cover change from 1985 to 2020 - iMap World 1.0," *Remote Sens. Environ.*, vol. 258, 2021, Art. no. 112364, doi: 10.1016/j.rse.2021.112364.
[98] C. Liu, X. Huang, Z. Zhu, H. Chen, X. Tang, and J. Gong, "Automatic extraction of built-up area from ZY3 multi-view satellite imagery: Analysis of 45 global cities," *Remote Sens. Environ.*, vol. 226, pp. 51–73, 2019, doi: 10.1016/j.rse.2019.03.033.
[99] D. L. Balk, U. Deichmann, G. Yetman, F. Pozzi, S. I. Hay, and A. Nelson, "Determining global population distribution: Methods, applications and data," *Adv. Parasitol.*, vol. 62, pp. 119–156, 2006, doi: 10.1016/S0065-308X(05)62004-0.
[100] P. Gong, X. Li, and W. Zhang, "40-Year (1978–2017) human settlement changes in China reflected by impervious surfaces from satellite remote sensing," *Sci. Bull.*, vol. 64, no. 11, pp. 756–763, 2019, doi: 10.1016/j.scib.2019.04.024.
[101] A. Hoffman-Hall, T. V. Loboda, J. V. Hall, M. L. Carroll, and D. Chen, "Mapping remote rural settlements at 30 m spatial resolution using geospatial data-fusion," *Remote Sens. Environ.*, vol. 233, 2019, Art. no. 111386, doi: 10.1016/j.rse.2019.111386.
[102] X. Li et al., "Mapping global urban boundaries from the global artificial impervious area (GAIA) data," *Environ. Res. Lett.*, vol. 15, no. 9, Aug. 2020, Art. no. 094044, doi: 10.1088/1748-9326/ab9be3.
[103] J. Yin et al., "Integrating remote sensing and geospatial big data for urban land use mapping: A review," *Int. J. Appl. Earth Observ. GeoInf.*, vol. 103, 2021, Art. no. 102514, doi: 10.1016/j.jag.2021.102514.
[104] J. Hird, E. DeLancey, G. McDermid, and J. Kariyeva, "Google earth engine, open-access satellite data, and machine learning in support of large-area probabilistic wetland mapping," *Remote Sens.*, vol. 9, no. 12, 2017, Art. no. 1315, doi: 10.3390/rs9121315.
[105] H. Tamiminia, B. Salehi, M. Mahdianpari, L. Quackenbush, S. Adeli, and B. Brisco, "Google earth engine for geo-big data applications: A meta-analysis and systematic review," *ISPRS J. Photogrammetry Remote Sens.*, vol. 164, pp. 152–170, 2020, doi: 10.1016/j.isprsjprs.2020.04.001.
[106] S. Saha, F. Bovolo, and L. Bruzzone, "Change detection in image time-series using unsupervised LSTM," *IEEE Geosci. Remote Sens. Lett.*, vol. 19, 2022, Art. no. 8005205.
[107] U. Khusni, H. I. Dewangkoro, and A. M. Arymurthy, "Urban area change detection with combining CNN and RNN from sentinel-2 multispectral remote sensing data," in *Proc. IEEE 3rd Int. Conf. Comput. Inf. Eng.*, Sep. 2020, pp. 171–175, doi: 10.1109/IC2IE50715.2020.9274617.
[108] D. Chianucci and A. Savakis, "Unsupervised change detection using spatial transformer networks," in *Proc. IEEE Western New York, Image Signal Process. Workshop*, 2016, pp. 1–5, doi: 10.1109/WNYIPW.2016.7904833.
[109] Z. Zheng, Y. Zhong, S. Tian, A. Ma, and L. Zhang, "ChangeMask: Deep multi-task encoder-transformer-decoder architecture for semantic change detection," *ISPRS J. Photogrammetry Remote Sens.*, vol. 183, pp. 228–239, 2022, doi: 10.1016/j.isprsjprs.2021.10.015.
[110] Z.-H. Zhou, "A brief introduction to weakly supervised learning," *Nature Sci. Rev.*, vol. 5, no. 1, pp. 44–53, 2018, doi: 10.1093/nsr/nwx106.
[111] D. Hao, L. Zhang, J. Sumkin, A. Mohamed, and S. Wu, "Inaccurate labels in weakly-supervised deep learning: Automatic identification and correction and their impact on classification performance," *IEEE J. Biomed. Health Informat.*, vol. 24, no. 9, pp. 2701–2710, Sep. 2020.
[112] Y. Li, L. Zhang, W. Wei, and Y. Zhang, "Deep self-supervised learning for few-shot hyperspectral image classification," in *Proc. IEEE Int. Geosci. Remote Sens. Symp.*, 2020, pp. 501–504.

Huiqun Ren received the M.S. degree in geomatics engineering from the Beijing University of Civil Engineering and Architecture, Beijing, China, in 2020. She is currently working toward the Ph.D. degree in photogrammetry and remote sensing from the School of Remote Sensing and Information Engineering, Wuhan University, Wuhan, China.

Her research interests include land cover/land use mapping and change detection.

Yu Liu received the M.S. degree in cartography and geographic information engineering from Beijing Normal University, Beijing, China, in 2018. He is currently working toward the Ph.D. degree in electronic information from Xidian University, Xi'an, China.

He is working with the Key Laboratory of Aerospace Information Application, CETC, Shijiazhuang, China. His main research interests include deep learning on remote sensing.

Xiaoyu Chang received the B.S. degree in surveying and mapping engineering from Southeast University, Nanjing, China, in 2017, and the M.S. degree in photogrammetry and remote sensing from Wuhan University, Wuhan, China, in 2020.

He is working with the Key Laboratory of Aerospace Information Application, CETC, Shijiazhuang, China. His research interests include remote sensing image understanding, semantic segmentation, and change detection.

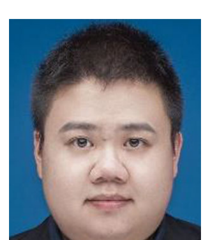

Jie Yang received the B.S. degree in remote sensing science and technology from the China University of Geosciences, Wuhan, China, in 2016. He is currently working toward the Ph.D. degree in photogrammetry and remote sensing from the School of Remote Sensing and Information Engineering, Wuhan University, Wuhan.

His research interests include land cover/land use mapping and change detection.

Xiao Xiao received the M.S. degree in environmental engineering from the School of Resource and Environmental Sciences, Wuhan University, Wuhan, China, in 2019.

She is working with the Spatial Information Technology Application Department, Changjiang River Scientific Research Institute, Wuhan. Her research interests include application of water conservancy remote sensing.

Xin Huang (Senior Member, IEEE) received the Ph.D. degree in photogrammetry and remote sensing from Wuhan University, Wuhan, China, in 2009.

He is working with the State Key Laboratory of Information Engineering in Surveying, Mapping and Remote Sensing. He is currently a Full Professor with Wuhan University, where he teaches remote sensing, image interpretation, etc. He is the Head of the Institute of Remote Sensing Information Processing (IRSIP), School of Remote Sensing and Information Engineering, Wuhan University. He has published more than 200 peer-reviewed articles (SCI papers) in the international journals. His research interests include remote sensing image processing methods and applications.

Dr. Huang has been supported by The National Program for Support of Top-notch Young Professionals (2017), the China National Science Fund for Excellent Young Scholars (2015), and the New Century Excellent Talents in University from the Ministry of Education of China (2011). He was the recipient of the Boeing Award for the Best Paper in Image Analysis and Interpretation from the American Society for Photogrammetry and Remote Sensing (ASPRS) in 2010, the John I. Davidson President's Award from ASPRS in 2018, and the National Excellent Doctoral Dissertation Award of China in 2012. In 2011, he was recognized by the IEEE Geoscience and Remote Sensing Society (GRSS) as the Best Reviewer of IEEE Geoscience and Remote Sensing Letters. He was the winner of the IEEE GRSS Data Fusion Contest in the years of 2014 and 2021. He was the lead guest editor of the special issue for the IEEE Journal of Selected Topics in Applied Earth Observations and Remote Sensing, the *Journal of Applied Remote Sensing*, *Photogrammetric Engineering and Remote Sensing*, and *Remote Sensing*. He was an Associate Editor of the *Photogrammetric Engineering and Remote Sensing* (2016–2019), an Associate Editor of the IEEE Geoscience and Remote Sensing Letters (2014–2020), an Associate Editor of the IEEE Journal of Selected Topics in Applied Earth Observations and Remote Sensing (2018–2022), and has been serving as an Associate Editor of the IEEE Transactions on Geoscience and Remote Sensing since 2022. He has also been an editorial board member of the Remote Sensing of Environment since 2019.